ACS OMEGA

http://pubs.acs.org/journal/acsodf

Article

Interactions of Nanoscale Self-Assembled Peptide-Based Assemblies with Glioblastoma Cell Models and Spheroids

Charlotta G. Lebedenko, Molly E. Murray, Beatriz G. Goncalves, Diego S. Perez, Dominic J. Lambo, and Ipsita A. Banerjee*

Cite This: *ACS Omega* 2023, 8, 12124−12143

Read Online

ACCESS | Metrics & More | Article Recommendations | Supporting Information

ABSTRACT: Peptide nanoassemblies have garnered remarkable importance in the development of novel nanoscale biomaterials for drug delivery into tumor cells. Taking advantage of receptor mediated recognition of two known peptides, angiopep-2 (TFFYGGSRGKRNNFKTEEY) and A-COOP-K (ACGLSGLC10 VAK) that bind to the over-expressed receptors low density lipoprotein (LRP-1) and fatty acid binding protein (FABP3) respectively, we have developed new peptide conjugates by combining the anti-inflammatory, antitumor compound azelaic acid with angiopep-2, which efficiently self-assembled into nanofibers. Those nanofibers were then functionalized with the A-COOP-K sequence and formed supramolecular hierarchical structures that were found to entrap the chemotherapeutic drug doxorubicin efficaciously. Furthermore, the nanoassemblies were found to release the drug in a dose-dependent manner and showed a stepwise increase over a period of 2 weeks under acidic conditions. Two cell lines (U-87-MG and U-138-MG) were utilized as models for glioblastoma cells grown in the presence of serum and under serum-free conditions to mimic the growth conditions of natural tumors. The drug entrapped assemblies were found to inhibit the cell proliferation of both U-87 and U-138MG glioblastoma cells. Three dimensional spheroids of different sizes were grown to mimic the tumors and evaluate the efficacy of drug release and internalization. Our results indicated that the nanoassemblies were found to have higher internalization of DOX and were well-spread throughout the spheroids grown, particularly under serum-free conditions. The nanoassemblies also displayed blood−brain barrier penetration when tested with a multicellular in vitro model. Such self-assembled nanostructures with targeting ability may provide a suitable platform for the development of new peptide-based biomaterials that can provide more insights about the mechanistic approach for drug delivery for not only 2D cell cultures but also 3D tumoroids that mimic the tumor microenvironments.

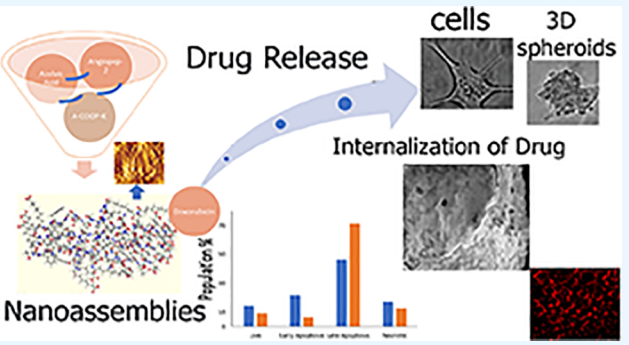

1. INTRODUCTION

Tumor targeting using specific peptide sequences is garnering importance due to the ability to selectively target tumor cells. In particular, a multi-receptor targeting approach is key due to the heterogeneous nature of tumors.[1] Additionally, tumor-related antigens, which are often part of plasma membrane receptors, provide avenues to specifically target tumors. For example, in a recent study, multivalent vector proteins were developed for simultaneously targeting IL-13RA2, EphA2, EphA3 and EphB2 receptors in glioblastoma tumors.[2−4] Glioblastoma is often characterized by high vascular endothelial cell proliferation, necrosis, and numerous genetic alterations, which make the tumor difficult to treat.[5−7] The standard treatment includes surgery, followed by radiotherapy and chemotherapy, but the success rate remains low.[8] Due to low survival rates, there is a pressing demand for improved and novel technologies that target glioblastoma tumors for imaging and treatment.[9]

Tumor targeting peptides that target receptors overexpressed on cell surfaces show great potential for the treatment of central nervous system (CNS) related cancers by receptor-mediated transcytosis of drugs across the blood−brain barrier (BBB).[10−22] The BBB restricts the passage of most molecules into the CNS, including several anticancer drugs, and is located in the endothelial cells of brain microvascular capillaries, which are connected by tight junctions.[23−26]

To overcome this, several nanoscale hybrid materials have been developed to improve drug delivery. For example, in a recent study, a tumor penetrating peptide that targets cell

Received: December 19, 2022
Accepted: March 3, 2023
Published: March 22, 2023

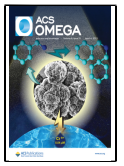

surface p32, LinTT1 (AKRGARSTA) was functionalized with iron oxide nanoparticles and utilized to target glioblastoma. The nanoparticles showed colocalization with tumor macrophages and lymphatic vessels and resulted in increased delivery of silver nanoparticles and albumin-paclitaxel nanoparticles. Furthermore, the nanoparticles exerted antiglioma activity in two cell models of glioblastoma.[27] In another study, Zhang and co-workers developed polyethylene glycol−polylactic acid (PEG−PLA) nanoparticles conjugated to the tumor homing cyclic peptide CGLIIQKNEC (CLT1) as a drug delivery system for targeting the extracellular matrix protein fibronectin, which is overexpressed in gliomas and is known to promote malignancy.[28] The nanoparticles were found to penetrate into the core of glioma spheroids and showed a strong inhibition of glioma spheroid growth and wide distribution within the spheroids. In a recent review regarding theranositc nanoparticles, Chen and co-workers discussed the importance of nanoparticle morphology and the effects of nanoparticles under physiological conditions, particularly within the tumor microenvironment.[29] They have highlighted the importance of modulating tumor microenvironments and optimizing nanoparticle properties for enhancing tumor penetration.[30]

In the realm of receptor targeted delivery, the peptide angiopep-2 selectively targets LRP1 (low density lipoprotein receptor-related protein 1 receptor),[31] which is derived from the Kunitz domains of aprotinin. In the CNS, LRP1 is highly expressed in neurons, activated astrocytes, microglia, endothelial cells and in the choroid plexus of the BBB.[32−34] Although LRP1 is expressed in healthy brain tissue, it is overexpressed in glioblastoma, making it a common target for therapeutics.[35−37] Angiopep-2 (TFFYGGSRGKRNNFKTEEY) is known to effectively cross the BBB through LRP1-mediated transcytosis.[38] In previous studies, this peptide has been directly conjugated to chemotherapeutic drugs such as paclitaxel, doxorubicin, and etoposide.[39−44] Angiopep-2-PEG-PE/amphotercin B polymeric micelles have also been developed as drug delivery vehicles that showed improved CNS permeability of amphotericin B for preventing fungal infections in the brain.[45] In another study, gold nanoprisms were functionalized with PEG and angiopep-2. The materials were found to efficiently cross the BBB and did not show toxicity both in vitro and in vivo.[46]

In addition to LRP1, the fatty acid binding protein 3 (FABP3) receptor, also known as the mammary-derived growth inhibitor (MDGI) is known to be overexpressed in glioma cells.[47−50] It has been shown that FABP3 expression is crucial for glioma cell viability as a regulator of lysosomal integrity.[51] Silencing of FABP3 in glioma spheroids led to cells being more susceptible to lysosomal membrane permeabilization (LMP) and cell death. In a study conducted by Ayo and co-workers, the glioblastoma homing peptide COOP (CGLSGLGVA) was discovered from phage display library and was found to bind to FABP3.[52] It was then found through alanine scanning that the binding interactions of COOP with FABP3 were further improved when the sequence was modified to A-COOP-K (ACGLSGLGVAK).[53] In previous work, COOP peptides have been shown to direct various chemotherapeutics and drug delivery vehicles to glioblastoma tumors,[54,55] though thus far relatively fewer studies with A-COOP-K-based drug delivery vehicles have been conducted.

To mediate drug delivery into tumor cells derived from glioblastoma and to 3D spheroids, in this work, we developed new peptide-based amphiphilic nanoassemblies where we incorporated both angiopep-2 and A-COOP-K into the same assembly. We hypothesized that taking advantage of receptor-mediated transport of both these peptides simultaneously would aid in targeting of tumor cells. To develop the peptide amphiphilic nanoassemblies, we first conjugated azelaic acid (Az) to angiopep-2 and self-assembled it into Aze5-angiopep-2 nanoassemblies. Azelaic acid is a dicarboxylic acid with seven methylene groups connecting the two carboxylic acid groups at each end, and has been shown to promote self-assembly of amphiphilic peptide-based nanomaterials.[56,57] Furthermore, azelaic acid has been shown to display antiproliferative activity against melanoma cell lines and leukemia cell lines.[58,59] However, to our knowledge, azelaic acid-conjugated nanoassemblies have never been investigated for targeting glioblastoma cell lines. The Aze5-angiopep-2 nanoassemblies were then functionalized with A-COOP-K peptide for targeting of two glioblastoma cell models, namely, U-87-MG and U-138-MG glioblastoma cells. Both these cell lines have been utilized as models for examining glioblastoma cell interactions in previous studies.[60,61] Supramolecular nanofibrillar structures were formed that efficiently entrapped the chemotherapeutic drug doxorubicin (DOX) and the interactions of the drug entrapped nanoassemblies with glioblastoma cells were examined. Furthermore, three-dimensional spheroids of the cells were grown, and the internalization of the drug entrapped nanoassemblies was explored. In previous work, it has been shown that the in vitro growth of cancer stem cells can be promoted by growth in serum-free media with supplements.[62] Furthermore, it has been demonstrated that growth under serum-free conditions allows for the sustenance of the phenotype and tumorigenicity of brain tumor stem cells.[63] Thus, spheroids were grown in both the presence and the absence of serum to assess if there were differences in uptake. Our results indicated that the nanoassemblies showed a two-step drug release at pH 5.8. Additionally, the drug entrapped assemblies were found to inhibit the growth of cells similar to DOX and the drug was found to be well dispersed in 3D spheroids. Furthermore, the nanoassemblies showed LRP1-mediated internalization and were found to be permeable through an in vitro BBB model. Thus, we have developed a new peptide-based drug delivery system that can potentially deliver chemotherapeutic drugs to 3D tumor microenvironments of glioblastoma cells with an enhanced efficacy.

2. MATERIALS AND METHODS

2.1. Materials. Angiopep-2 (TFFYGGSRGKRNNFKTEEY) and A-COOP-K (ACGLSGLCVAK) peptides were custom-ordered from GenScript. Doxorubicin was purchased from Cayman Chemical Company (Ann Arbor, MI, USA). 5-Carboxy-X-rhodamine *N*-succinimidyl ester and flow cytometry staining buffer were obtained from ThermoFisher Scientific (Waltham, MA, USA). *N*-Hydroxysuccinimide (NHS), 1-ethyl-3-(3-(dimethylamino)propyl)carbodiimide (EDAC), azelaic acid, glutaraldehyde, and dimethylformamide (DMF) were purchased from Sigma-Aldrich (St. Louis, MO, USA). Eagle's minimum essential medium (EMEM) with L-glutamine, 1× Dulbecco's phosphate buffered saline (PBS), and human glioblastoma U-87-MG cell line (HTB-14), U-138-MG cell line (HTB- 16), and fetal bovine serum (FBS) were purchased from ATCC (Manassas, VA, USA). Primary mouse neurons E18-E19 C57/BL6 (mouse brain) were purchased from Neuromics. Trypsin-EDTA 1× was purchased from ThermoFisher Scientific. Sodium citrate and sodium chloride

https://doi.org/10.1021/acsomega.2c08049
ACS Omega 2023, 8, 12124−12143

were purchased from Fisher Scientific. Serum-free Neurobasal Plus medium with the B-27 Plus supplement was purchased from ThermoFisher Scientific. Human blood−brain barrier modeling kit and human brain endothelial cells were purchased from Science Cell Research Laboratories.

2.2. Methods. *2.2.1. Preparation of Aze5-Angiopep-2 Conjugate.* The Aze5-angiopep-2 conjugate was prepared according to previously established peptide coupling methods.[64] Briefly, azelaic acid (0.025 M) was dissolved in dimethylformamide (DMF). To activate its side chain carboxylic acid groups, EDAC (0.015 M) and NHS (0.015 M) were added. The solution was allowed to shake at 100 rpm for 1 h at 4 °C. Then angiopep-2 (TFFYGGSRGKRNNFKTEEY) (0.005 M) peptide was added to the solution and stirred at 4 °C for 24 h, after which the solvent was rotary evaporated under vacuum. The product obtained was then recrystallized with acetone and dried using a speed-vac concentrator before further analysis. The formation of the product was confirmed by ^{1}H NMR spectroscopy. The sample was analyzed using a Bruker 400 NMR in DMSO-d_6 solvent that contained 0.3% TMS. Peaks were seen at δ 1.1 (d, 6H); δ 1.3 (m, 14H); δ 1.4 (m, 20H); δ 1.6 (m, 28H); δ 1.8 (q, 8H); δ 2.0 (m, 6H); δ 2.1 (t, 2H); δ 2.2 (m, 8H); δ 2.4 (t, 4H); δ 2.9 (d, 4H); δ 3.0 (t, 4H); δ 3.1 (d, 2H); δ 3.3 (t, 4H); δ 3.4 (d, 8H); δ 4.1 (s, 6H); δ 4.3 (t, 8H); δ 4.5 (t, 1H); δ 4.6 (q, 2H); δ 4.7 (t, 1H); δ 4.8 (t, 2H); δ 4.9 (t, 4H); δ 5.2 (s, 3H); δ 6.5 (s, 4H); δ 6.6 (d, 4H); δ 6.9 (d, 4H); δ 7.1 (s, 4H); δ 7.2 (m, 15H); δ 7.7 (s, 2H); δ 7.9 (s, 2H); δ 8.4 (s, 18H); δ 9.0 (s, 5H).

2.2.2. Self-Assembly of Aze5-Angiopep-2 Conjugates. The product obtained was self-assembled under aqueous conditions at 25 °C. Briefly, the conjugate (0.01 M) was allowed to self-assemble for 7 days in deionized water. The growth of the assemblies was monitored by dynamic light scattering analysis. The assemblies were then dried under a vacuum before further analysis.

2.2.3. Incorporation of A-COOP-K with Nanoassemblies. To the Aze5-angiopep-2 nanoassemblies, EDAC (0.05 M), and NHS (0.05 M) were added to promote binding with the A-COOP-K peptide (ACGLSGLGVAK) (0.05 M), and the mixture was allowed to stir overnight. The A-COOP-K bound to Aze5-angiopep-2 assemblies was washed and centrifuged with deionized water to remove any unbound A-COOP-K. Samples were then stored at 4 °C for further analysis.

2.2.4. Drug Encapsulation. In order to determine the optimal concentration of drug that could be entrapped within the nanoassemblies, we examined varying concentrations of the drug and carried out entrapment studies with the Aze5-angiopep-2 bound A-COOP-K assemblies. The concentration of doxorubicin (DOX) was varied between a 0.005 and 0.065 mM. To examine entrapment, four sets were prepared. Each set contained 2 mg/mL of Aze5-angiopep-2 bound A-COOP-K assemblies which were incubated with either 0.005 0.020, 0.040, or 0.065 mM concentrations of DOX. The samples were shaken for 3 min, and the absorbance at 482 nm was immediately measured to determine the initial absorbance of DOX using UV−vis spectrophotometry taken with the Thermo Scientific NanoDrop 2000c spectrophotometer. The samples were allowed to shake at 50 rpm for 72 h at 4 °C and then centrifuged for 3 h at 10000*g*. The absorbances of the supernatants for each sample were then taken. The encapsulation efficiency was calculated using the following equation.

$$\text{entrapment efficiency (\%)} = (\text{absorbance DOX initial} - \text{absorbance DOX supernatant}) / (\text{absorbance DOX initial}) \times 100$$

The supernatants of each of the samples were then removed, and the drug entrapped Aze5-angiopep-2 bound A-COOP-K assemblies were then vacuum-dried, weighed, and stored at 4 °C in the dark before drug release studies.

2.2.5. Drug Release Studies. Each of the drug entrapped assemblies was reconstituted in 500 μL of pH 5.8 phosphate buffer solution to mimic the tumor microenvironment, and absorbance readings were taken. For the first 30 min, readings were taken every 10 min, then every 30 min. For each reading, 2 μL of sample was utilized and immediately replaced with 2 μL of buffer, so the total volume remained constant. Readings were taken over a course of 2 weeks to determine the release pattern of the drug. To determine the concentration of drug released, the molar absorptivity coefficient of DOX was calculated from a standard curve. The molar absorptivity coefficient was found to be 13,329 L/mol/cm.

2.2.5.1. Differential Scanning Calorimetry (DSC) Analysis. To further confirm the incorporation of the drug into the nanoassemblies, we carried out a DSC analysis. Each sample (3.2 mg) was weighed into a hermetic aluminum sample pan and then sealed tightly with a lid. Samples were then loaded into a Q200 DSC instrument (TA Instruments). Prior to insertion of the sample, the instrument was cooled to 0 °C under nitrogen. The thermal phase transition of each sample was recorded up to 280 °C. Each sample was run three times to ensure reproducibility.

2.3. Cell Studies. *2.3.1. 2D Cultures.* U-87-MG and U-138 glioblastoma cell lines were cultured in Eagle's minimum essential medium (EMEM, Quality Biological) composed of 10% fetal bovine serum (ATCC), 3 mL of 1x antibiotic-antimycotic mixture per 500 mL EMEM (GIBCO), 10 units/mL penicillin, and 10 μg/mL streptomycin (GIBCO). The cells were incubated at 37 °C in a 5% CO_2 incubator. Cells were grown to confluence, and the medium was changed every 2 to 3 days. Cells were split twice a week. Cells were also grown in serum-free media to mimic genetic and phenotype changes that occur in tumor cell populations.[65] Briefly, cultures of U-87-MG and U-138 cells were grown in serum-free neuronal basal media with a B27 supplement and 3% antibiotic−antimycotic mixture. Cells were grown to confluence as before, and the medium was changed every 2 days. We also examined the effects of the nanoassemblies on noncancer cells with primary mouse neurons grown in primary mouse neural culture medium, (Neuromics) which is a serum-free DMEM/F12-based medium containing L-glutamine, HEPES, penicillin, and streptomycin. The medium was supplemented with Culture Media Supplement (Catalog #M37106, Neuromics).

2.3.2. ELISA. Human FABP3 and LRP1 ELISA assay kits (HU FABP3 ELISA kit and LRP1 ELISA kit) were purchased from ThermoFisher scientific and Cell Biolabs, respectively, and used to measure FABP3 and LRP1 levels for cells grown in the presence of serum and in serum-free media cultures according to the manufacturer's instructions. Absorbance was measured at 450 nm by using a Biotek plate reader.

2.3.3. Cytotoxicity Studies. U-138-MG, U-87-MG glioblastoma cells, and primary mouse neurons were plated at a density of 1×10^4 cells/well in 96-well plates and allowed to

https://doi.org/10.1021/acsomega.2c08049
ACS Omega 2023, 8, 12124−12143

spread for 24 h in a 37 °C incubator under 5% CO_2 conditions. Cells grown under serum-free conditions and in the presence of serum were tested. After 24 h, nanoassemblies as well as DOX loaded nanoassemblies were incubated with the cells at concentrations of 2 μM or 10 μM. The amount of DOX control utilized was calculated to be equivalent to a final concentration of 2 μM or 10 μM in the well plates to maintain consistency. In addition, we also examined controls which included neat angiopep-2 (10 μM), A-COOP-K (10 μM) peptides and untreated cells. After 24 h, MTT reagent[66] was added to each well and allowed to incubate for 4 h. Next, the crystal dissolving solution was added to each well, and the well plate was incubated for another 4 h. The absorbance of each well was then analyzed using the Biotek Eon plate reader at 560 and 590 nm. This procedure was repeated in triplicate. Statistical analysis was carried out using Student's t tests to determine p values.

2.3.4. Annexin V FITC–Propidium Iodide Assay Using FACS Analysis. As a proof of concept, U-87-MG cells were plated at a density of 1×10^5 cells/well and incubated at 37 °C in 5% CO_2 in 24-well plates. After 36 h of incubation, nanoassemblies, DOX loaded nanoassemblies, DOX control, as well as neat angiopep-2 and A-COOP-K peptides were incubated with the cells at concentrations of 2 μM and 10 μM each at 37 °C in 5% CO_2 incubator for 18 h. Then the medium was aspirated from each well and transferred to sterilized centrifuge tubes and each well was washed with 1× PBS free of calcium and magnesium ions. Then cells were trypsinized to detach the adherent cells after which the trypsin was removed and replaced with the media. The contents of the flask were then transferred into sterile centrifuge tubes. Cells were then centrifuged at 250g for 8 min. The supernatant was discarded and the cells were resuspended in media and centrifuged again. After the supernatant was discarded, Annexin V Binding Buffer diluted to 1× was added to resuspend the cells as per the protocol (Cayman Chemicals). Then 5 μL of FITC-labeled Annexin V and 5 μL of nuclear staining solution (propidium iodide) was added to the cell suspension. After vortexing for a minute, the cells were incubated for 20 min at room temperature in the dark and then analyzed immediately using flow cytometry.[67] The BD FACSMelody flow cytometer was set to read the samples at excitation of 488 nm and emission of 525 nm for the Annexin V FITC staining solution and 655–730 emission for the propidium iodide staining solution. Each study was carried out in triplicate. Flow cytometry data were then analyzed on FlowJo v10.8.

2.3.5. Antibody Labeling and Cellular Uptake. In order to examine LRP1- and FABP3-mediated cellular uptake of angiopep-2 and A-COOP-K peptides, as well as the nanoassemblies, FACS analysis was performed. These experiments were performed on U-87 and U-138 cell lines grown in serum-free neuronal basal medium with B27 supplement as per previously established protocols.[68] Cells were plated at a density of 1×10^4 cells per well in 6-well plates and were allowed to spread for 4 h in a 5% CO_2, 37 °C incubator. For antibody labeling, the cells were then incubated with either LRP1 or FABP3 antibodies in separate wells. To test for LRP1-mediated internalization, we added the diluted primary antibody (LRP1 recombinant rabbit monoclonal) in a ratio of 1:50 followed by an incubation period of 3 h in a shaker at 5% CO_2, 37 °C incubator. Then the secondary antibody, Alexa Fluor 488 anti-rabbit IgG, was also diluted 1:50, added to cells, and incubated with the cells for 24 h. Then the medium was aspirated off and replaced with fresh media, and cells were incubated with the nanoassemblies or angiopep-2 (10 μM) for another 24 h. The medium was then aspirated off and replaced with PBS, and then trypsin was added to detach the cells. The cells were then transferred to individual eppendorf tubes and spun at 10,000g for 5 min. The supernatant was decanted and the pellet was resuspended in FACS buffer which was then passed through a filter cap onto FACS tubes and analyzed at an appropriate wavelength of excitation for alexa fluor (488 nm). A similar procedure was carried out for FABP3 labeling of antibodies, where the plated cells were directly incubated with diluted Coralite 594-conjugated FABP3 mouse antibody (50 μL) prior to incubation with A-COOP-K peptide (10 μM) or nanoassemblies (10 μM), followed by trypsinization after 24 h of incubation. The cells were then transferred to individual Eppendorf tubes and spun at 10,000g for 5 min. The supernatant was decanted, and the pellet was resuspended in FACS buffer which was then passed through a filter cap onto FACS tubes and excited at 582 nm using a BD FACSMelody flow cytometer.

2.4. Blood–Brain Barrier (BBB) Coculture Model and Permeability. To examine if the nanoassemblies were capable of permeating the BBB, we utilized a triple coculture BBB model in which primary human brain microvascular endothelial cells (Science Cell Research laboratories), human brain vascular pericytes, and human astrocytes were cultured together in a Transwell system.[69] First, the basolateral side of the collagen coated inserts (Transwell, polycarbonate membrane, 3 μm pore size, Corning Costar, USA) was coated with poly-L-lysine (1.5 μg/cm^2). The inserts were placed in a 24-well plate, and the plate containing inserts was then kept in an incubator at 37 °C in 5% CO_2 for 1 h. The plate was then removed, and the inset was washed twice with 18Ω water to remove any residual poly-L-lysine and then the water was aspirated off. The Transwell inserts were then flipped inside the well plate and seeded with astrocyte cells (5×10^4 cells) on the basolateral side of the coated inserts and incubated in a 5% CO_2 incubator at 37 °C for 3 h to allow the astrocytes to adhere. After the incubation period, the inserts containing astrocytes were inverted and placed inside the well plate containing 500 μL of 2D-BBB coculture medium with 2D BBB supplement (Science Cell Research laboratories) and FBS. Then 2D-BBB coculture medium (500 μL) was added to the apical side of the inset. The well plate was then placed in the 5% CO_2 incubator for 24 h at 37 °C, after which the inserts were inverted again onto the lid of the well plate. To prepare the coculture model, pericytes were then seeded (2.0×10^4 cells/cm^2) to the basolateral side of tissue culture inserts. Once adhered, the insets were put back to the well plates containing 2D-BBB coculture medium (500 μL) with 2D BBB supplement and FBS inside the wells and within the inserts. These were then placed back into the 5% CO_2 incubator and allowed to reach 90% confluence for 3 days. Then the medium inside the inserts (apical side) was aspirated followed by seeding with 6.0×10^4 cells/cm^2 of human brain endothelial cells followed by the addition of 2D BBB medium to the apical side. Then the inserts containing the cells on the two sides of the membrane insert were placed back into the 24-well plates. The three cell types were cocultured for 4 days before permeability experiments. The tightness of the BBB coculture model was verified by measurement of transendothelial electric resistance (TEER) by an EVOM volt-ohm meter (World Precision

https://doi.org/10.1021/acsomega.2c08049
ACS Omega 2023, 8, 12124–12143

Instruments, Sarasota, FL, USA) combined with STX-2 electrodes. TEER of coated, but cell-free, inserts were subtracted from measured TEER values. When appropriate TEER values (210 ± 4 Ω.cm^2) were obtained, the model was used for experiments.

Before beginning the permeation experiments, serum-free 3D-basal medium along with 3D growth supplement coculture medium (500 μL) was added inside the wells and within the inserts and allowed to sit in the 37 °C, 5% CO_2 incubator for 1 h. Then the medium was aspirated off and replaced with DMEM/F12 supplemented with 1% FBS and treated in the upper/donor compartment (500 μL) with the rhodamine-labeled nanoassemblies (2 and 10 μM) diluted in phenol red-free DMEM/F12 supplemented with 1% FBS. Rhodamine labeling of nanoassemblies was carried out prior to these studies by conjugating the nanoassemblies with 5-carboxy-X-rhodamine *N*-succinimidyl ester in a 1:1 ratio and incubating for 24 h, followed by centrifugation and washing with 18Ω water to remove any unbound dye. To test the function of the BBB model, the flux of permeability marker molecules such as sodium fluorescein and rhodamine-B-labeled bovine serum albumin was also determined. Experiments were carried out in triplicate each. Immediately after treatment, 5 μL of sample was collected from the lower/acceptor compartments and the upper (donor) compartments and placed in 100 μL of PBS in a Costar black opaque 96-well plate. Each sample was read separately using a Biotek Synergy H1 microplate reader, which was set up to read at an excitation at 540 nm and emission at 570 nm. In the case of the sodium salt of fluorescein, samples were excited at 488 nm, and emission was recorded at 520 nm. Readings were repeated every 30 min until the fluorescence readings from upper chamber and lower chamber of the inset began to reach similar levels, indicating that an equilibrium had been established.

To quantitatively determine the permeability, we calculated the volume cleared (VC) using the equation VC = ($F_{Lower} \times V_{Lower}$)/$F_{Upper}$ where F_{lower} and F_{Upper} correspond to the fluorescence intensity of the sample in the lower and upper chambers. The V_{lower} is the volume of the lower chamber, which was kept constant (500 μL) for the calculations. Then, to obtain the permeability coefficient (P), we utilized the equation Pcell+filter = PSS as described in previous methods.[70] To obtain the permeability surface area (PS) product, we plotted the VC against time and determined its slope. The PS was then divided by s, the culture area of the filters (0.47 cm^2).

2.5. Statistical Analysis. Data are presented as the standard error of the mean (SEM) or standard deviation (SD). Statistical analyses were performed using GraphPad Prism 8 software (Graphpad PRISM 5, Graphpad Software Inc., San Diego, CA, USA).[71] Means were compared using an unpaired t test. All experiments were repeated at least three times (n = 3).

2.6. 3D Cultures. *2.6.1. Preparation of Spheroids.* U-87-MG or U-138-MG glioblastoma cells were grown as monolayers on an adherent 75 cm^2 cell culture flask until 70% confluence was obtained. We grew cells in both serum-free (neuronal basal medium with B27 supplement) and in EMEM media supplemented with FBS. These were then washed with 1× PBS followed by trypsinization and were incubated for 5 min in a humidified atmosphere at 37 °C and 5% CO_2 incubator. The trypsin was then replaced with serum-free neuronal basal media with B27 supplement or with EMEM. The contents of the flask were then transferred to one 15 mL polypropylene centrifuge tube and spun at 500g for 10 min. The supernatant was then discarded, and 3 mL of media were added to resuspend the pellet. Cells were then transferred to U-shaped low attachment Nunclon Sphera Corning spheroid microplates (24-well) to initiate spheroid formation.[72] Two different densities of cells were plated: 4000 cells/well and 10,000 cells/well. Cells were imaged every day using optical microscopy and the medium was changed every 3 days by slightly raising the plate from one end to avoid aspirating the spheroids. The growth of the spheroids was monitored by optical microscopy over a period of 10 days. Spheroids were imaged at various magnifications using an inverted phase contrast Amscope IN480TC-20MB13 microscope or SEM.

2.6.2. Delivery of Doxorubicin into Spheroids. We treated six day old spheroids grown in the presence and absence of serum (both U-87-MG and U-138-MG cell lines) with DOX loaded nanoassemblies (10 μM) and DOX (10 μM) and incubated the spheroids with the drug or drug loaded nanoassemblies. To study delivery of DOX, each of the treated samples was then washed with PBS to remove unassociated DOX entrapped nanoassemblies or neat DOX. They were then transferred to glass slides carefully in PBS buffer and analyzed using an AmScope phase contrast inverted fluorescence microscope with 10× objective using 560−580 nm emission filter. Quantitative measurements were carried out using ImageJ software,[73] where areas of specific dimensions within the spheroid image was selected to quantify the fluorescence intensity of DOX, which correlated with the spheroid penetration. The Corrected Total Fluorescence intensity was plotted against the distance from the periphery for all treatments.

2.6.2.1. Calcein Assay. To further examine the effect of the nanoassemblies entrapped with Dox, on the viability of the spheroids, a Calcein-AM staining assay was performed.[74] As a proof of concept, we utilized six day old spheroids for this study. The spheroids were incubated with the DOX entrapped nanoassemblies (10 μM) and neat DOX (10 μM) for 24 h. After treatment, the spheroids were transferred into a fresh culture plate (24-well) and washed with 1× assay buffer three times, and the spheroids were stained with Calcein-AM (3 μM) solution and incubated at 37 °C for 1 h. The spheroids were then imaged by using an inverted fluorescence microscope (Amscope) to detect green fluorescence at 480 nm excitation.

2.7. Characterization. *2.7.1. Absorbance Spectroscopy.* UV−vis spectroscopy of the DOX entrapped nanoassemblies as well as dye-conjugated peptides and nanoassemblies was performed using a Thermo Scientific NanoDrop 2000c UV−vis spectrophotometer in the range of 190−800 nm. For drug release studies, the peak at a wavelength of 482 nm was monitored to determine the release profile of the DOX.

2.7.2. Fourier Transform Infrared (FTIR) Spectroscopy. FTIR spectroscopy was carried out for confirmation of the incorporation of the A-COOP-K peptide with the Aze-5-angiopep-2 assemblies as well as the formation of the Aze-5-angiopep-2 assemblies. Additional FTIR spectroscopy was also conducted to confirm the entrapment of DOX. We recorded spectra at range of 1000−4000 cm^{-1} using a ThermoFisher Scientific Nicolet iS50 FTIR. In general, 100 scans per sample was carried out.

2.7.3. Atomic Force Microscopy. Atomic force microscopy (AFM) was utilized to determine the morphologies of the self-assembled Aze5-angiopep-2 assemblies before and after

https://doi.org/10.1021/acsomega.2c08049
ACS Omega 2023, 8, 12124−12143

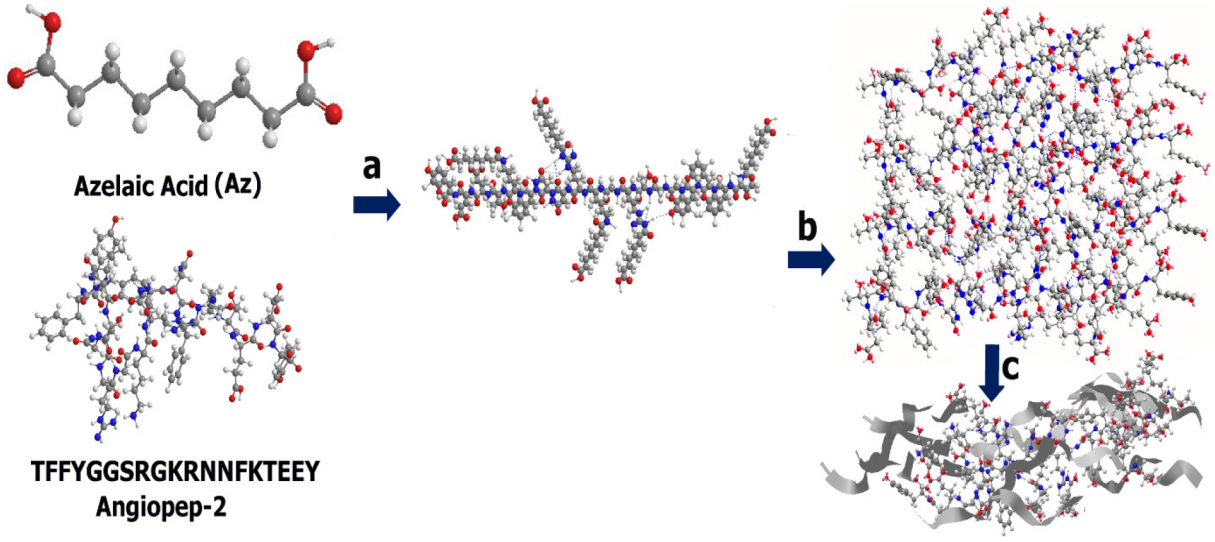

Figure 1. Scheme for formation of A-COOP-K bound Aze5-angiopep-2 bound nanofibers. (a) NHS/EDC in DMF, followed by isolation of product. (b) Self-assembly of the Aze5-angiopep-2 conjugate under aqueous conditions for 1 week. (c) Coupling of A-COOP-K with the self-assembled Aze5-angiopep-2 nanoassemblies to form ACOOP-K bound Aze4-angiopep-2 nanofibers using NHS-EDC (red = oxygen; blue = nitrogen; and gray = carbon). The ribbon structure is representative of the A-COOP-K peptide. Dotted lines show H-bonding interactions.

incorporation of the A-COOP-K peptide as well as after entrapment of DOX. Samples were diluted in water, placed on mica sheets, and air-dried before analysis. Images were captured at multiple locations in contact mode on a Bruker multimode 8 atomic force microscope using a CONTV cantilever, with a frequency of 13 kHz, spring constant of 0.2 N/m, and tip radius of 10 nm.

2.7.4. Circular Dichroism (CD) Spectroscopy. CD spectroscopy was utilized to analyze the secondary structures of the Aze5-angiopep-2 nanoassemblies before and after incorporation of A-COOP-K. Samples were prepared in deionized water and vortexed for two min before analysis. Samples were analyzed in the far-UV region (190−260 nm) using a Jasco J-1500 CD spectrometer. All of the readings were performed in triplicate.

2.7.5. Fluorescence Microscopy. We performed fluorescence microscopy using an inverted AmScope 1500X phase contrast inverted fluorescence microscope with camera, IN480TC-FL-MF and U2-RFLT 100 digital control box. Samples were viewed at various magnifications and excited at an appropriate wavelength. Images were captured using Amlite software and analyzed to evaluate interactions of the nanoassemblies and DOX with both 2D U-87-MG and U-138-MG glioblastoma cells and 3D spheroids grown in the presence and absence of serum.

2.7.6. Fluorescence-Activated Cell Sorting (FACS) Flow Cytometry. A BD FACSMelody flow cytometer was used for the analysis of cellular uptake and apoptosis. Flow cytometry employs multiple fluorochromes with varying emission and excitation wavelengths to distinguish populations of cells.[75] For each analysis, we prepared samples in FACS buffer consisting of 50 mL of 1× PBS, 1% bovine serum albumin, and 0.05% sodium azide and then filtered them through filter caps into FACS test tubes to be loaded into the instrument. Based on the densities of cells present in each sample, the event rate recorded by the instrument was optimized by adjusting the flow rate. The number of events recorded for each experiment was set on the basis of the frequency of the cell population of interest. The experiment with samples containing a high frequency of cell populations was recorded for 20,000 events. We kept the total number of events consistent for each experiment so that data could be compared between samples. The results of each experiment were then analyzed using FlowJo v10.8 software.

2.7.7. Fluorescence Spectroscopy. Fluorescence spectroscopy was carried out by using a Jobin Yvon Fluoromax 3 fluorescence spectrometer. Samples were excited at appropriate wavelengths, and the emission spectrum was collected for each sample.

2.7.8. Scanning Electron Microscopy (SEM). Analyses of the nanoassemblies were carried out using a Zeiss EVO MA10 model SEM. Samples were dried on to carbon double stick conducting tapes and were examined at a range of 7 to 10 kV at varying magnifications in EP mode. To image the spheroids, silicon chips (Ted Pella) (5 mm × 5 mm) were irradiated with UV-light and washed with ethanol, dried and coated with poly-L-lysine. The chips were then washed with 18Ω water and placed in six-well plates. Five day old spheroids were then transferred to the chips carefully and allowed to adhere to the chips for 48 h in a 37 °C, 5% CO_2 incubator. The medium was then removed, and the spheroids were washed with PBS. The spheroids were then fixed with 2% glutaraldehyde in NaHCA buffer (30 mM HEPES, 100 mM NaCl, 2 mM $CaCl_2$) for 1.5 h at room temperature. The fixed spheroids were rinsed with PBS and then postfixed with 1% osmium tetroxide in PBS for 1 h at room temperature in the dark. The spheroids were then rinsed with distilled water and dehydrated stepwise at room temperature, through 5 min washes with 10, 25, 50, 75, 95, and 100% ethanol. The samples were air-dried and the spheroids were then imaged by placing the silicon chip on to the SEM stub using a carbon double stick tape.

3. RESULTS AND DISCUSSION

3.1. Formation of Nanoassemblies. Peptide amphiphiles have been shown to form higher-ordered supramolecular structures based on the composition of their functional groups and growth conditions due to intra- and intermolecular interactions.[76] In this study, the dicarboxylic acid, azelaic

https://doi.org/10.1021/acsomega.2c08049
ACS Omega 2023, 8, 12124−12143

acid, was conjugated to the free amine groups of the peptide sequence TFFYGGSRGKRNNFKTEEY (angiopep-2) at the N-terminal of threonine as well as to the amino groups of the side chains of lysine and arginine to form the peptide amphiphile Aze5-angiopep-2. Figure 1 shows the scheme for the formation of the assemblies. As a proof of concept, four amphiphilic structures of Aze5-Angio-pep2 are shown to interact to form Aze5-angiopep-2 nanoassemblies in the scheme to demonstrate the self-assembly process. As can be seen the self-assembly was promoted by extensive H-bonding interactions as well as strong hydrophobic interactions. In addition, stacking interactions between the phenylalanine and tyrosine moieties also promote assembly. The self-assembled structures are functionalized with A-COOP-K to form the Aze5-angiopep-2 bound A-COOP-K assemblies. The incorporation of A-COOP-K was also promoted by H-bonding interactions with the Aze5-angiop-2 nanoassemblies.

To visualize the formation of the assemblies, we performed AFM. Upon self-assembly (Figure 2), Aze5-angiopep-2 was found to form nanoscale chain-like fibrous structures (Figure 2a). The average diameter was found to be 200 nm. The formation of these fibrillar structures was promoted by strong H-bonding interactions between the free carboxylic groups of azelaic acid end carboxyl groups and the C-terminal of the angiopep-2, as well as π-stacking interactions between the phenylalanine groups.[77] In addition, H-bonding interactions exist between the −C═O and NH groups. Furthermore, hydrophobic interactions between the long chain alkyl groups of the Aze5 moieties also aided in the formation of these assemblies.[78]

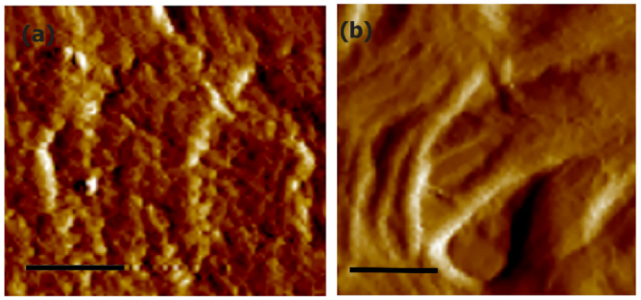

Figure 2. AFM topography images of (a) Aze-4-angiopep-2 nanofibers; (b) Aze4-angiopep-2-A-COOP-K nanoassemblies. Scale bar: 400 nm.

In previous work, it has been shown that polymetronidazole-polymethacrylate conjugates, which were incorporated with the lipid composite 1,2-distearoyl-*sn*-glycero-3-phosphoethanolamine-PEG (DSPE-PEG), lecithin, and angiopep-2-DSPE-PEG successfully self-assembled into nanoparticles by taking advantage of the hydrophobic core and hydrophilic amine groups and were utilized for drug delivery of Temozolomide into glioma cells.[79] It is expected that similar interactions occur in the case of the nanoassemblies due to the presence of hydrophobic and hydrophilic moieties. In another study, it was shown that angiopep-2-modified polyamidoamine (PAMAM) dendrimers were self-assembled into nanospheres effectively by taking advantage of inter- and intramolecular interactions of the dendrimer structures and were utilized for drug delivery into glioma cells.[80]

To facilitate targeting, we then conjugated the nanofibers with FABP3 receptor binding peptide A-COOP-K sequence ACGLSGLCVAK. The results were confirmed by AFM imaging, which showed the formation of dense fibrillary networks upon binding to the peptide as shown in Figure 2b. Upon incorporation of A-COOP-K into the aze5-angiopep-2 nanofibers, we observed the formation of thicker hierarchical structures, with layers of fibers wrapped around, which confirmed its incorporation. To further confirm the incorporation of the A-COOP-K peptide, we also conducted CD and FTIR spectroscopy. As shown in Figure 3, the individual angiopep-2 neat peptide and the A-COOP-K peptide displayed a random coil conformation. In previous work, it has been shown that angiopep-2 has been known to form random coil structures.[81] The formation of the Aze5-angiopep-2 assemblies resulted in a change in conformation where a mix of β-turn (as indicated by a broad positive peak at 220 nm and negative peaks at 209 and 204 nm and a positive peak at 198 nm[82]) and unordered conformation was observed. These results are consistent with previous studies where it has been shown that peptide amphiphiles with hydrophobic and hydrophilic regions

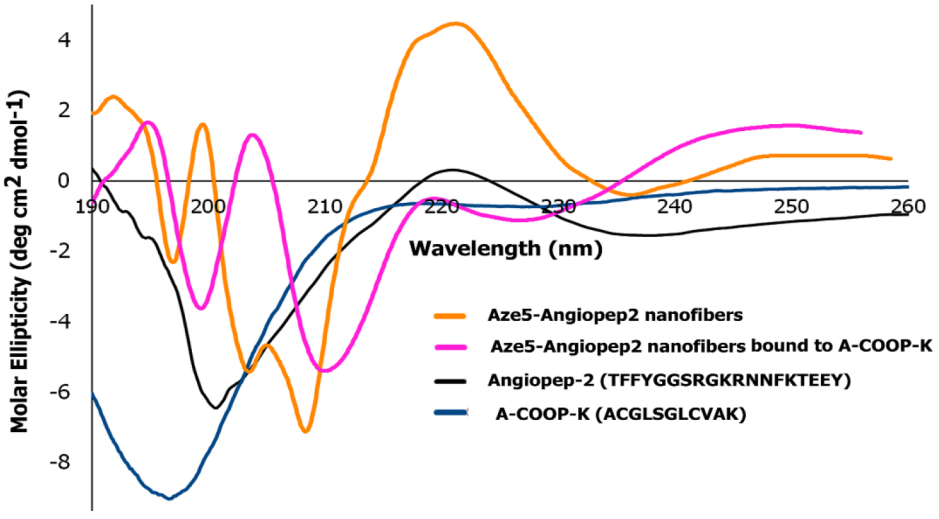

Figure 3. Comparison of CD spectra of nanoassemblies before and after incorporation of A-COOP-K, neat A-COOP-K peptide, and neat angiopep-2 peptide.

https://doi.org/10.1021/acsomega.2c08049
ACS Omega 2023, 8, 12124−12143

(similar to these assemblies) can adopt conformations where the coexistence of unordered structures and β-sheets can occur,[83] leading to the formation of stable fibrillary nanostructures. Upon incorporation of the A-COOP-K peptide, the Aze5-angiopep-2-A-COOP-K nanoassemblies showed shifts, though the β-turn features and unordered structure were maintained as indicated by the strong negative bands at 202 and 211 nm, while positive bands are seen at 194 and 205 nm. The intensity of the peak at 220 nm seen in the case of the angiopep-2 nanoassemblies was diminished. These changes confirm the incorporation of the A-COOP-K peptide. Similar changes were observed when peptide hydrogels consisting of short peptide sequences such as FFDKY was conjugated amphotericin B.[84]

The FTIR spectra (Supporting Information, Figure S1) show a comparison of the nanoassemblies before and after incorporation of A-COOP-K as well as that of the neat peptides. For the Aze5-angiopep-2 assemblies, a peak in the carbonyl region was observed at 1690 cm^{-1} due to amide I, and is indicative of a β-turn motif.[85] A short peak was observed at 1616 cm^{-1} due to aromatic C═C stretching, as expected for residues such as Tyr and Phe present in the angiopep-2 component of the assemblies. The amide II peak was found to be at 1516 cm^{-1}, while the C−H bending peak and C−O peaks were found to be at 1460 and 1203 cm^{-1}, respectively. A peak at 1127 cm^{-1} was indicative of C−O stretching due to serine, tyrosine, and threonine groups. Additional peaks were seen at 2940 and 2840 cm^{-1} due to aromatic and aliphatic C−H stretching. A broad −OH peak was seen at 3290 cm^{-1} (data not shown). Upon incorporation of the A-COOP-K peptide, we observed a shift in the peaks. As can be seen in the figure, the A-COOP-K bound to Aze5-angiopep-2 assemblies showed a relatively broad carbonyl peak in the amide I region between 1704 and 1640 cm^{-1} which is indicative of strong H-bonding interactions as well as the coexistence of random coil and β-turns.[86] The amide II peak was also shifted to 1531 cm^{-1}. The C−O stretching peaks were shifted to 1136 and 1198 cm^{-1} indicating their involvement in H-bonding. Additionally, the −OH stretching peak was found to be at 3293 cm^{-1} while the C−C stretching peaks were seen at 2931 and 2848 cm^{-1} (data not shown). These results confirm the incorporation of A-COOP-K. The results were compared with neat angiopep-2 and A-COOP-K peptides. The −C═O stretching peaks for the neat angiopep-2 peptide were seen at 1654 and 1624 cm^{-1} in the amide I region, while the amide II peak was seen at 1540 cm^{-1} with a shoulder at 1516 cm^{-1}. Overall the above results corroborated with previous work, where it was shown that a shift in FTIR peaks occurred particularly in the carbonyl region after combining angiopep-2 with other peptide moieties such as trileucine.[87] The neat A-COOP-K peptide on the other hand showed peaks at 1643 cm^{-1} in the amide I region and the amide II peak at 1524 cm^{-1} while the C−O peaks were seen at 1203 and 1143 cm^{-1} which are slightly shifted compared to those obtained for the assemblies due to inter- and intramolecular interactions and functionalization.

3.2. Drug Entrapment. After the formation of the A-COOP-K bound Aze5-angiopep-2 assemblies, the chemotherapeutic drug DOX was then entrapped within the assemblies. To determine the most optimum concentration of the drug that could be entrapped, four different concentrations were examined which included 0.005 0.020, 0.040, and 0.065 mM concentration of DOX. The encapsulation efficiency was found to be concentration-dependent and was found to be 24, 36, 57, and 76%, respectively. These results indicate that DOX was successfully entrapped within the assemblies. We also confirmed the entrapment of DOX by using FTIR spectroscopy, AFM imaging and DSC analysis. As shown in Figure 4, the FTIR

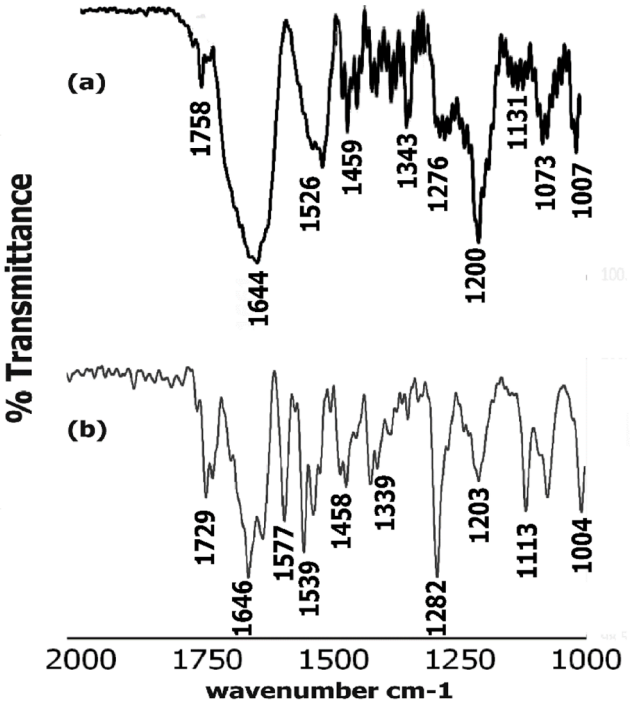

Figure 4. (a) Comparison of FTIR spectra of (a) DOX entrapped nanoassemblies and (b) neat DOX.

spectrum of neat DOX showed distinct peaks at 1729 cm^{-1} with a shoulder at 1715 cm^{-1} as well as a peak at 1646 cm^{-1} due to the presence of carbonyl group.[88] A peak at 1620 cm^{-1} due to the C═C groups of the aromatic ring system is also seen. Strong peaks are seen at 1577 cm^{-1} and 1539 cm^{-1} due to C−C ring stretching and −NH bending vibrations, respectively. The $-CH_2$ bending peak is seen at 1458 cm^{-1}, while −C−O stretching peaks are seen at 1282 and 1203 cm^{-1} along with strong peaks at 1113 and 1004 cm^{-1} due to the presence of secondary alcohol groups of DOX. Additionally, strong peaks are observed at 2849 cm^{-1} and 2916 cm^{-1} due to aliphatic and aromatic C−H stretching, respectively, along with a broad −OH peak at 3304 cm^{-1} due to −OH stretching, and the −NH stretching peak was seen at 3648 cm^{-1} (data not shown). In comparison, A-COOP-K bound Aze5-angiopep-2 assemblies entrapped with DOX showed a broad peak at 1644 cm^{-1} with a short shoulder at 1662 cm^{-1} in the carbonyl region along with a short peak at 1758 cm^{-1}, which is slightly shifted compared to neat DOX. Similar broadening and reduction in FTIR peak intensity were seen when DOX was entrapped in ammonium palmitoyl glycol chitosan polymeric nanostructures due to entrapment of DOX within the nanoassemblies.[89] The amide II peaks were found to be at 1526 cm^{-1} with a shoulder at 1536 cm^{-1}. Furthermore, peaks are also seen at 1459 cm^{-1} and 1343 cm^{-1}. The C−O−C peak is seen at 1276 cm^{-1} and the C−O peak due to the glycosyl group of DOX is seen at 1073 cm^{-1}. The broad −OH stretching peak seen for DOX was shifted to 3280 cm^{-1}, while the $-NH_2$ peak was shifted to 3401 cm^{-1} implying H-bonding interactions with the nano-

https://doi.org/10.1021/acsomega.2c08049
ACS Omega 2023, 8, 12124−12143

assemblies. The aromatic and aliphatic C−H stretching peaks were seen at 2952 and 2850 cm^{-1}, respectively (data not shown).

To further confirm the incorporation of DOX into the assemblies, we conducted AFM imaging (Figure 5). As shown,

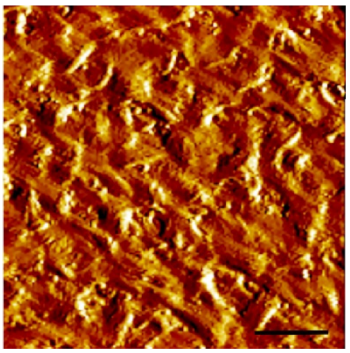

Figure 5. AFM image of DOX entrapped nanoassemblies. Scale bar = 1 μm.

distinct changes were observed upon incorporation of DOX. Upon incorporation of DOX, a multilayered structure is observed with multiple areas of larger aggregates encompassed within a porous mesh, signifying the incorporation of DOX (Figure 5). The formation of such aggregated structures upon incorporation of DOX is expected given that DOX itself has a tendency to form dimers or trimers and aggregates under aqueous conditions depending upon concentration.[89] Overall it is likely that the incorporation of DOX into A-COOP-K bound Aze5-angiopep-2 assemblies is promoted by strong H-bonding interactions between the −C═O groups of DOX and the −NH groups of the peptide moieties of the assemblies; in addition to H-bonding between the −OH groups of serine and angiopep-2 (from A-COOP-K) and DOX. Stacking interactions between the aromatic ring system of DOX and the phenylalanine and tyrosine groups of angiopep-2 is also likely to enhance its interaction with DOX. Similar interactions were found to enhance complexation of DOX with other drug binding peptides[90] containing fragments such as WXXW that mimic the hydrophobic regions of P-glycoproteins, and the tryptophan residues aid in noncovalent hydrophobic interactions with doxorubicin, while X could be any amino acid.

To further confirm drug entrapment in the assemblies, we conducted DSC analysis. As shown in Figure 6, the neat Aze5-angiopep-2-A-COOP-K nanoassemblies showed a sharp endothermic peak at 166.4 °C indicative of thermal melting followed by a short, broad endothermic peak at 176.3 °C, which most likely corresponds to the degradation of the peptide nanoassemblies. As expected, DOX showed a single sharp endothermic peak at 219 °C, which corresponds to its melting point. The DOX entrapped in Aze5-angiopep-2-A-COOP-K nanoassemblies, however, showed a peak corresponding to the melting of Aze5-angiopep-2-A-COOP-K at 167.2 °C followed by additional short peaks at 173 and 182 °C due to degradation of the assemblies. We also observed a peak corresponding to the melting point of DOX at 220 °C, which confirmed that DOX was successfully entrapped within the assemblies. Similar trends have been seen when chitosan entrapped galantamine drug was entrapped in chitosan nanoparticles where a relatively broad endothermic peak is seen for the drug entrapped nanostructures.[91]

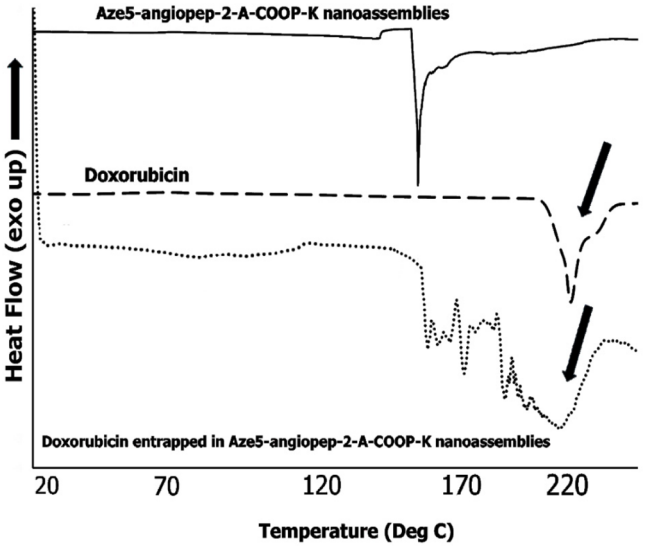

Figure 6. Comparison of DSC thermograms of Aze5-angiopep-2-A-COOP-K nanoassemblies before and after entrapment with DOX. Arrows indicate the melting point of DOX.

3.4. Drug Release Studies. To ensure that Aze5-angiopep-2 bound A-COOP-K nanoassemblies are capable of releasing the drug over time, drug release studies were conducted. The results obtained are shown in Figure 7. To

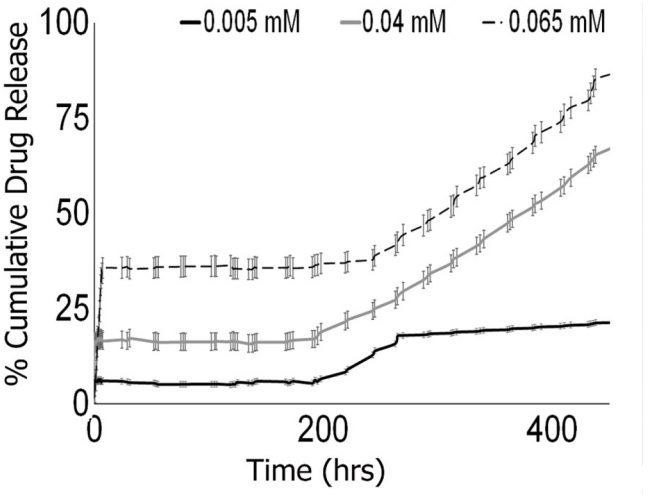

Figure 7. Comparison of release of DOX at various concentrations from the nanoassemblies over a period of 450 h. Error bars indicate standard deviations.

mimic the tumor microenvironment conditions, release studies were carried out at pH 5.8.[92] As shown, overall, the release of the drug was found to be concentration-dependent. The percent cumulative release data shows a burst release initially for DOX encapsulated at 0.065 mM followed by a steady release up to 240 h. However, at 240 h, an increase in release was observed reaching 87% at 450 h. This indicates a stepwise release. The burst release initially seen at the higher concentration of the drug is likely due to diffusion of the drug from outer surfaces of the fibrous nanoassemblies,[93] followed by a slow, and gradual degradation of the peptide-based nanoassemblies from the outermost regions to innermost parts of the mesh. Thus, a greater amount of drug may

https://doi.org/10.1021/acsomega.2c08049
ACS Omega 2023, 8, 12124−12143

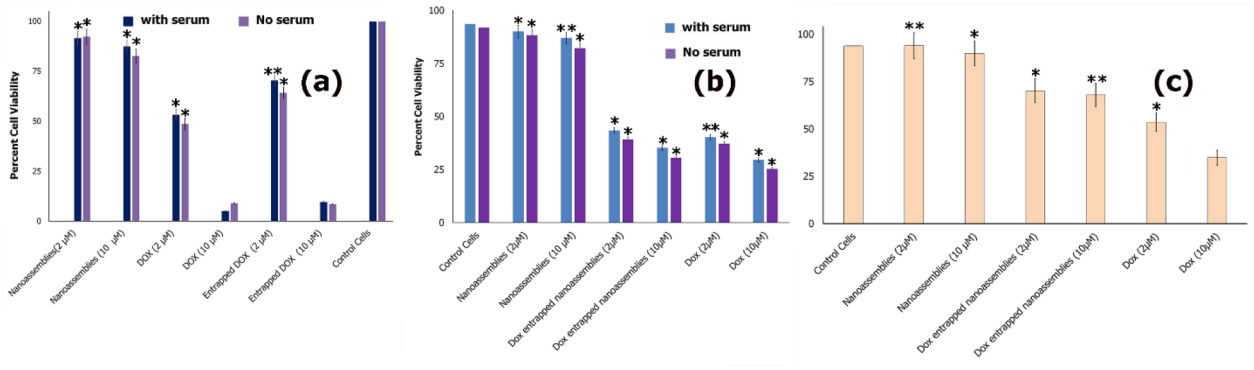

Figure 8. (a) Comparison cell viability of U-87-MG cells grown in the presence and absence of serum after 24 h of incubation with DOX entrapped nanoassemblies, neat nanoassemblies, and neat DOX compared to the untreated cells. (b) Comparison cell viability of U-138-MG cells grown in the presence and absence of serum after 24 h of incubation with DOX entrapped assemblies, neat nanoassemblies and neat DOX. (c) Comparison cell viability of mouse neuronal cells after 24 h of incubation with DOX entrapped nanoassemblies, neat nanoassemblies and neat DOX. The data were obtained from three independent experiments. The values represent the mean values for $n = 3$, $^{*}p < 0.05$ and $^{**}p < 0.001$. Statistical analysis was carried out according to a Student's t test.

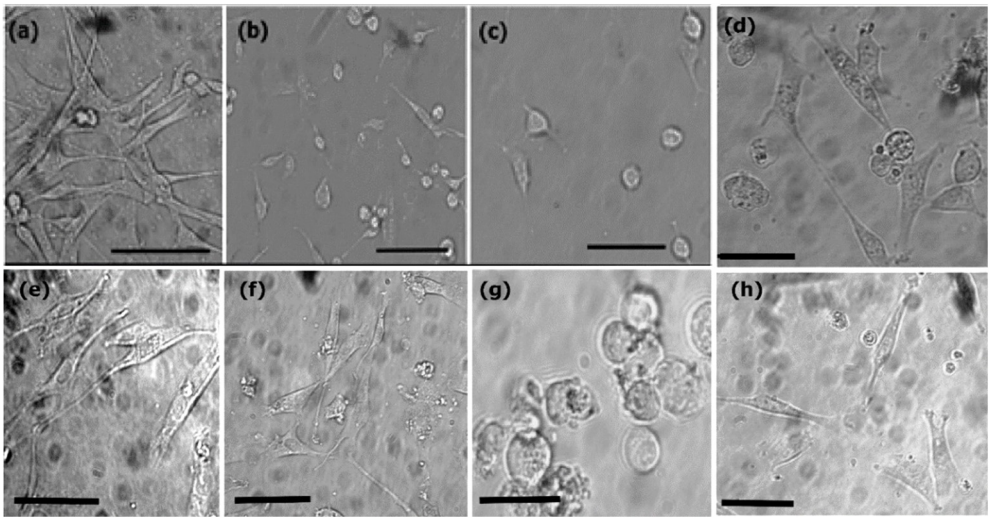

Figure 9. Top Row: Optical microscopy images of U-87-MG cells after 24 h of incubation with various constructs: (a) control cells; (b) cells after treatment with 10 μM DOX entrapped Aze5-angiopep-2-A-COOP-K nanoassemblies; (c) DOX-treated assemblies; (d) cells grown in serum-free media. Scale bar = 20 μM. Bottom Row: Optical microscopy images of U-138-MG cells after 24 h of incubation with various constructs: (e) control cells; (f) cells after treatment with 10 μM DOX entrapped Aze5-angiopep-2-A-COOP-K nanoassemblies; (g) DOX-treated assemblies (10 μM); (h) cells grown in serum-free media. Scale bar = 20 μm.

potentially remain within the inner cores of the cross-linked network mesh for a longer period of time, which is released as the assemblies degrade. Such stepwise drug release systems may be advantageous due to their biodegradability, particularly in an acidic microenvironment like tumors, which may be conducive for the assemblies to unfold. Such stepwise drug release has been observed in the case of PEO-*b*-PCL (poly(ethylene oxide)-*b*-polycaprolactone) amphiphilic vesicles as well as silica nanoparticles capped with β-cyclodexrin coated with PEG.[94,95] At 0.04 mM concentration of the drug entrapped assemblies, a similar pattern of release is observed, though at 450 h, comparatively lesser drug (68%) was released which is expected, given that lesser drug was entrapped. Interestingly at the lowest concentration, a slower steady release is observed, and no burst release was seen. Additionally, after the first step release at 200 h, an increase in release was observed up to 280 h after which a steady release was seen with 22% of drug released at 450 h. At the lowest concentration of the drug, where the amount of nanoassemblies is higher, the drug may be entrapped and cross-linked within the matrices of the assemblies and may take significantly longer to release due to the biphasic release.[96] In previous studies, also it has been shown that polymeric fibrous matrices composed of polyvinylpyrrolidone and polycaprolactone showed an initial burst release followed by sustained release depending upon the concentrations of the components.[97] Overall, these results indicate that the DOX entrapped nanoassemblies may be potentially applicable for drug delivery.

3.5. Cell Studies. *3.5.1. 2D Cultures.* To examine the impact of the drug loaded nanoassemblies on U-87-MG and U-138-MG glioblastoma cells, cell viability studies using the MTT assay were conducted. As a control, viability studies were also carried out with nontumor cells (mouse neurons). U-138-MG and U-87-MG cells grown in the presence and absence of serum were tested. Results obtained after 24 h of incubation with various constructs are shown in Figure 8. As displayed in Figure 8a, for the U-87 cells, the results were comparable for the cells grown in the presence and absence of serum. The cells

https://doi.org/10.1021/acsomega.2c08049
ACS Omega 2023, 8, 12124−12143

showed slightly less viability for neat nanoassemblies at a higher concentration (82.5%) for cells grown without serum versus those grown in the presence of serum (87.5%). For the DOX entrapped nanoassemblies, viability was found to be 69.2% without serum at the lower concentration versus 73.3% in the presence of media with serum. Interestingly at higher concentration of the DOX entrapped assemblies, the viability was found to be 8.3% for cells grown in the absence of serum versus those grown in the presence of serum at 9.5%.

The results of neat DOX were comparable at the higher concentration, implying that the drug was released into the cells. However, at the lower concentration, cells treated with neat DOX showed lower viability compared to drug entrapped assemblies due to slower release of the drug. Upon comparing the results with the U-138-MG cells (Figure 8b), we observed that at 2 μM concentration, the drug entrapped assemblies caused reduction in cell viability (43.2% for cells grown in the presence of serum and 39.5% for those grown in the absence of serum), while at 10 μM the viability was reduced to 35.3% and 30% respectively. The results were comparable to those obtained for neat DOX. These results indicate that the drug is likely being internalized into U-87-MG cells more efficiently than into U-138-MG cells. Overall the neat Aze5 angiopep-2-A-COOP-K nanoassemblies were found to show slightly lower proliferation compared to control cells, likely due to the presence of Aze moieties, which in past studies have been shown to be cytotoxic to tumor cells. We also examined the cytotoxicity with noncancerous cells (mouse neurons) to ensure that the delivery was targeted. Our results showed that the DOX entrapped nanoassemblies showed relatively less cytotoxicity for those cells compared to the tumor cells, and the viability was found to be ~65%. While DOX alone showed higher cytotoxicity (27.2% viability) at 10 μM concentration versus 49.3% at lower concentration (2 μM). This is expected given that neat DOX does not distinguish between tumor cells and nontumor cells while the nanoassemblies are expected to be relatively more targeted toward tumor cells.

To further explore the effect of the nanoassemblies, phase contrast optical microscopy was conducted. As shown in Figure 9, the optical microscopy images show a difference in morphology before and after treatment with the drug entrapped nanoassemblies and the neat drug in both cell models. The untreated cells appeared healthy with a stellate morphology, indicating that they are motile. This is consistent with the expected morphologies of U-87-MG and U-138-MG cells seen in past studies.[98−100] Upon treatment with DOX entrapped nanoassemblies, fewer cells with elongated, stellate morphologies were seen, and a number of cells appeared rounded and showed signs of blebbing, which corroborated the results found from the MTT assay. Higher number of cells appeared to be rounded up for the U-87-MG cells compared to U-138-MG cells. In the case of DOX-treated samples, the cells were all mostly rounded up, indicative that the cells were no longer viable for both cell lines. These results further confirm that the DOX entrapped nanoassemblies may be releasing the drug relatively slowly, which may be advantageous over a longer period of time due to sustained release. Nevertheless, the drug entrapped assemblies reduce the proliferation and viability of U-87-MG and U-138-MG glioblastoma cells. We also compared the morphologies of both cell lines grown in serum-free media. As shown in the figure, overall both cell lines displayed elongated appearance, though overall the growth was found to be slower in serum-free media compared with cells grown in the presence of serum.

3.5.2. Expression of FABP3 and LRP1 Proteins. To detect if the U-87-MG and U-138-MG cell lines that were utilized as models for glioblastoma cells expressed endogenous LRP1 and FABP3 receptors, enzyme linked immunoassays were conducted for the detection and quantitation of LRP1 and FABP3 in the cell samples. LRP1 was detected with an anti-LRP1 antibody followed by HRP-conjugated secondary antibody, while a biotin-conjugated antibody to human FABP3 was attached to streptavidin-HRP for the detection of FABP3. Results were compared with the standard curves obtained by conducting serial dilutions with the standard solution of LRP1 and FABP3-treated antibodies separately. The concentration of FABP3 was determined to be 0.175 ng/mL ± 0.8 ng/mL FABP3 protein for the U-87-MG cell line in the presence of serum, while 0.253 ± 0.2 ng/mL FABP3 protein was observed for cells grown without serum. The U-138-MG cells displayed concentrations of 0.282 ± 0.3 ng/mL of FABP3 protein in the presence of serum and 0.412 ± 0.1 ng/mL in the absence of serum. The LRP1 concentration for U-87-MG cells was found to be 0.932 ± 0.5 ng/mL in the presence of serum and 0.992 ± 0.6 ng/mL for cells grown in the absence of serum. The LRP1 expression in U-138-MG cells showed a concentration of 0.601 ± 0.4 ng/mL in the presence of serum and 0.702 ± 0.3 ng/mL in the absence of serum. These results show that LRP1 expression is lower in the case of U-138-MG cells. It is well-known that higher LRP1 expression is seen in U-87-MG cell lines compared to U-138-MG cells, as indicated by the human protein atlas which provides information about the spatial map of the human proteome,[101] thus our results corroborated with previous work. The results also indicate that the U-87-MG cells show a higher expression of LRP1 receptor protein compared to FABP3, which is expected for U-87-MG cell lines.[102] It is also noted that both cell lines showed a relatively low FABP3 expression. This is likely because higher FABP3 expression occurs when these cell lines are grown under hypoxic conditions.[103] In addition, a slightly higher expression of both receptors was observed under serum-free conditions as expected. The histogram showing the data obtained for ELISA is shown in the Supporting Information (Figure S2).

We then examined if the nanoassemblies were capable of receptor-mediated internalization using FACS analysis (Figure 10). Because relatively higher expression of the receptors was observed for the cells grown in neuronal basal media with B-27 supplement without serum, we utilized cells grown under serum-free conditions for the internalization studies. As seen in Figure 10a,b, the cells treated with the nanoassemblies showed higher LRP1-mediated internalization in the case of both U-138-MG and U-87-MG cell lines compared with control cells. However, angiopep-2 alone showed higher internalization comparatively as expected given that it is a smaller peptide compared to the nanoassemblies. Nevertheless, it is interesting to note that the nanoassemblies also displayed LRP1-mediated internalization. In comparison, no FABP3-mediated internalization was observed (Figure 10c,d). This may be due to relatively lower expression of endogenous FABP3 receptor compared to LRP1. However, it is to be noted that A-COOP-K peptide alone also did not show internalization. These results corroborate with previous studies conducted by Ayo and co-workers, who demonstrated that while A-COOP-K is a glioblastoma tumor homing peptide, it does not successfully internalize into U-87-MG cells through endogenous FABP3

https://doi.org/10.1021/acsomega.2c08049
ACS Omega 2023, 8, 12124−12143

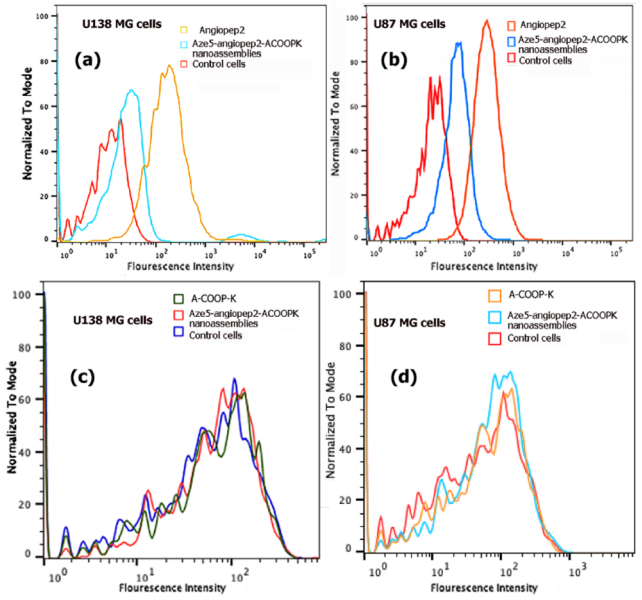

Figure 10. (a) U-138-MG cells; (b) U-87-MG cells. Top Row: LRP1-mediated internalization. Each cell line was labeled with primary antibody, LRP1 (recombinant rabbit monoclonal) followed by secondary antibody, Alexa Fluor 488 anti-rabbit IgG, followed by treatment with AngioPep2, or nanoassemblies for 6 h before analysis. Bottom Row: (c) U-138-MG cells; (d) U-87-MG cells. FABP3-mediated internalization was tested by labeling the cells with Coralite 594-conjugated FABP3 mouse antibody followed by treatment with A-COOP-K, or nanoassemblies for 6 h before analysis.

receptors due to very low receptor expression.[53] They showed that internalization is seen only in the case of cells transfected with FABP3.

3.6. In Vitro BBB Model Permeability. In order to ascertain if the nanoassemblies can penetrate the BBB, permeation of the nanoassemblies across an in vitro coculture model of BBB grown with human pericytes, brain endothelial cells, and astrocytes was explored. The scheme for the preparation of the BBB model is shown in Scheme 1. We first examined the tightness of the coculture model by exploring the penetration of the small molecule permeability indicator (sodium salt of fluorescein) and a relatively large protein, bovine serum albumin across the BBB. The P_{app} (apparent permeability) of fluorescein and BSA was found to be relatively low (0.22×10^{-6} and 0.06×10^{-6} cm/s, respectively) (Figure 11). These values obtained were similar to previously published works.[104,105] A photograph of one of the wells of the BBB model prepared using Transwell inserts is shown in the inset of Figure 11. As seen, the permeation of the Rhodmaine-B-labeled nanoassemblies at 2 μM concentration resulted in a higher apparent permeability with P_{app} of 4.6×10^{-6} cm/s, while that of the nanoassemblies at 10 μM concentration showed an apparent permeability constant P_{app} of 2.7×10^{-6} cm/s across the BBB model. The values obtained are in the range seen for drugs such as cimetidine and digoxin, which have been studied using in vitro models of BBB.[106] Similar results have been observed for fluorescently labeled silica nanoparticles which showed permeability of the nanoparticles through an in vitro cocultured BBB model.[107] However, one must keep in mind that the ideal size and shape of nanoassemblies may need to be altered, given that the in vivo BBB structural integrity may be different. Other factors such as efflux transporters, and the overall homeostatic environment of the CNS will also need to be considered. Furthermore, the integrity of the BBB is lesser in a tumor tissue compared to healthy brain tissue, which may change the penetration rate and capability of the nanoassmblies.[108]

3.7. Apoptosis Studies. Apoptosis studies in the presence of DOX entrapped nanoassemblies were compared to the results obtained for neat DOX treated cells. These studies were carried out as a proof of concept with U-87-MG-treated cells to examine if apoptosis was one of the mechanisms for the reduction of cell viability. It is well-known that DOX induces apoptosis in cells,[109] and therefore it was investigated if the nanoassemblies that were entrapped with DOX could induce apoptosis using Annexin FITC-propidium iodide assay.[110] Each scatter plot in Figure 12 was obtained by gating on the FSC-A/SSC-A control pseudo color sample plot, followed by the FSC-A/FSC-W and SSC-A/SSC-W plots. The population within the gate of the latter was then plotted as Annexin FITC-A/Propidium Iodide-A and gated with a quadrant gate to quantify the frequency of each event. A biexponential scale was used to avoid events on the chart edges. The gates were then copied to the remaining samples. As shown in the figure, compared to the control cells which showed 98.5% of live cells, there is a shift toward the late apoptosis quadrant upon treatment with the DOX entrapped nanoassemblies (Figure 12a,b) which indicates that the DOX entrapped nanoassemblies are most likely inducing late apoptosis (46.5% at 2 μM and 71.4% at 10 μM). The number of necrotic cells was found to be 17.2% and 12.8%, respectively. Thus, the DOX entrapped assemblies successfully induced apoptosis in a dose-dependent manner on the U-87-MG cells. Comparatively, neat DOX (Figure 12c,d) showed higher numbers of late apoptotic cells, showing 68.9% late apoptotic and 7.2% necrotic at 2 μM and 52.7% late apoptotic in addition to 24% necrotic cells at 10 μM. Thus, in both cases, on average most cells were found to be in late-apoptotic stages after 24 h of incubation. When compared to the controls, which included untreated cells, neat nanoassemblies, and the neat peptides, as can be seen in the bottom row of Figure 12e–h, we observed the percent of live-cells was significantly higher as expected in all cases with the neat peptides angiopep-2 and A-COOP-K showing 96.9 and 98.2% live cells, while the Aze5-angiopep-2-A-COOP-K nanoassembly showed 87.6% live cells. The slightly lower number of live-cells in the case of the nanoassemblies is expected due to the Aze5 component, which has been known to induce cytotoxicity in tumor cells[111] at higher concentrations. Regardless, compared to the DOX entrapped cells, the cytotoxicity is significantly lower implying that apoptosis is seen primarily due to the DOX component. A graphical representation of the comparison of various populations of apoptotic, live and necrotic cells is also shown below the scatter plots.

3.8. 3D Cell Cultures. *3.8.1. Growth of Spheroids.* Given the results obtained from the 2D cultured cells, in order to mimic the 3D environment of tumoroids, spheroids were grown at varying cell densities. Three-dimensional tumor spheroid cultures not only establish similar gradients of nutrients, pH and oxygen as that of tumors but also have 3D cell–cell contact which can stimulate production of extracellular matrix proteins and enhanced intercellular communication that occur in a tumor matrix.[112] Thus, tumor spheroids were created with the U-87-MG cells and U-138-MG cells in both serum-free media and media supplemented with serum

https://doi.org/10.1021/acsomega.2c08049
ACS Omega 2023, 8, 12124−12143

Scheme 1. Top: Optical Microscopy Images of 2D Cultures of (i) Astrocytes, (ii) Human Brain Endothelial Cells (Scale Bar = 20 μm), and (iii) Pericytes. Bottom: Schematic for Construction of the Well in Vitro BBB Model Using Transwell Inserts in 24-Well Plates

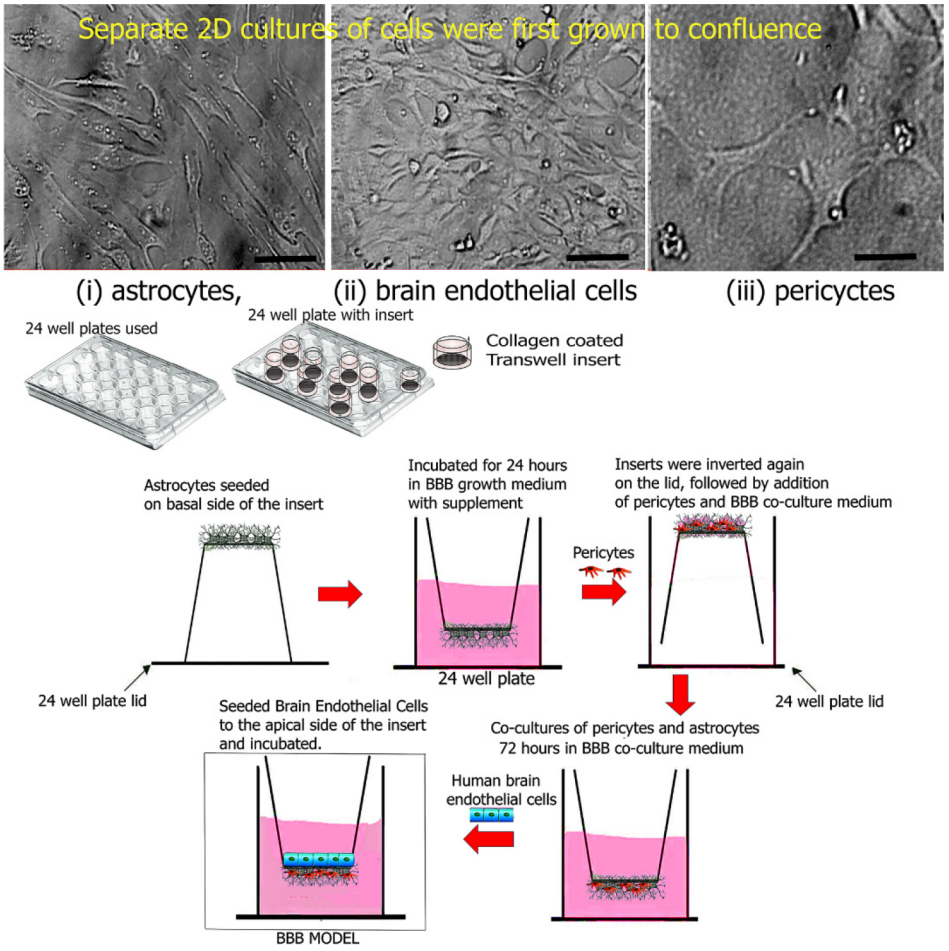

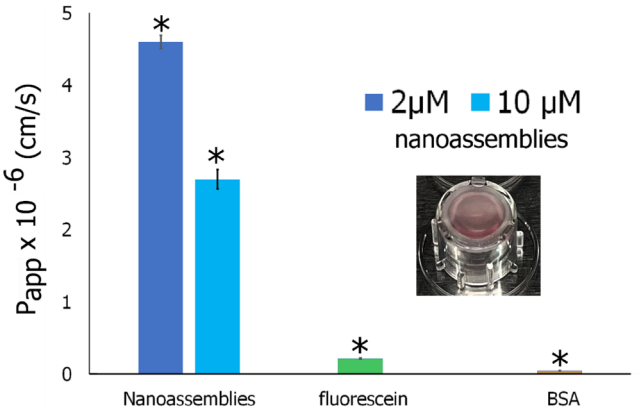

Figure 11. Plot of permeability coefficients of nanoassemblies at 2 and 10 μM concentration as well as controls Rhodamine-B-labeled BSA and sodium salt of fluoroscein, which was used as permeability marker. The P_{app} was calculated as given in the Methods section. Results are the mean ± SD (n = 3); *p < 0.05. Inset shows one of the wells showing BBB coculture model prepared and utilized in this study.

and the differences in morphology and growth were explored, as shown in Figure 13.

Cells seeded at different densities (4000 cells/well; 10,000 cells/well) in the presence and absence of serum were grown to investigate the impact of growth conditions. As seen in the figure, at each cell density, the spheroids continued to grow over time. In the case of U-87-MG cells grown in the presence of serum, the spheroids appear multilayered and attain a rounder appearance over time that is characteristic of spheroids.[106] Furthermore, with time, the spheroids appeared to fuse with neighboring smaller spheroids. The proliferating outer layer of cells forms a shell around the outside of the spheroid. Each spheroid also contained an inner core which contains live quiescent cells.[113] As the spheroids kept growing in size, the inner core started becoming darker, which likely represents necrotic cells as the oxygen supply and nutrients become scarcer.[100] Surrounding that necrotic layer are the quiescent cells, followed by the layer of proliferating cells on the outer surface.[114] At 10 days, in the case of cells grown at 4000 cells/well, the diameter was found to be 20 μm, with multiple spheroids of smaller sizes. At 10,000 cells/well, the sizes of the spheroids were approximately 90−100 μm. The growth of larger spheroids at higher cell densities is facilitated by the proximity of a larger number of cells, which enable higher cell−cell interaction and cell-matrix interaction at the larger densities of cells.[115] In comparison, U-87 spheroids grown under serum-free conditions had a less round morphology, particularly at higher density. Although the sizes were approximately similar to those grown in the presence of serum (25 and 80 μm), respectively, after 10 days of growth.

https://doi.org/10.1021/acsomega.2c08049
ACS Omega 2023, 8, 12124−12143

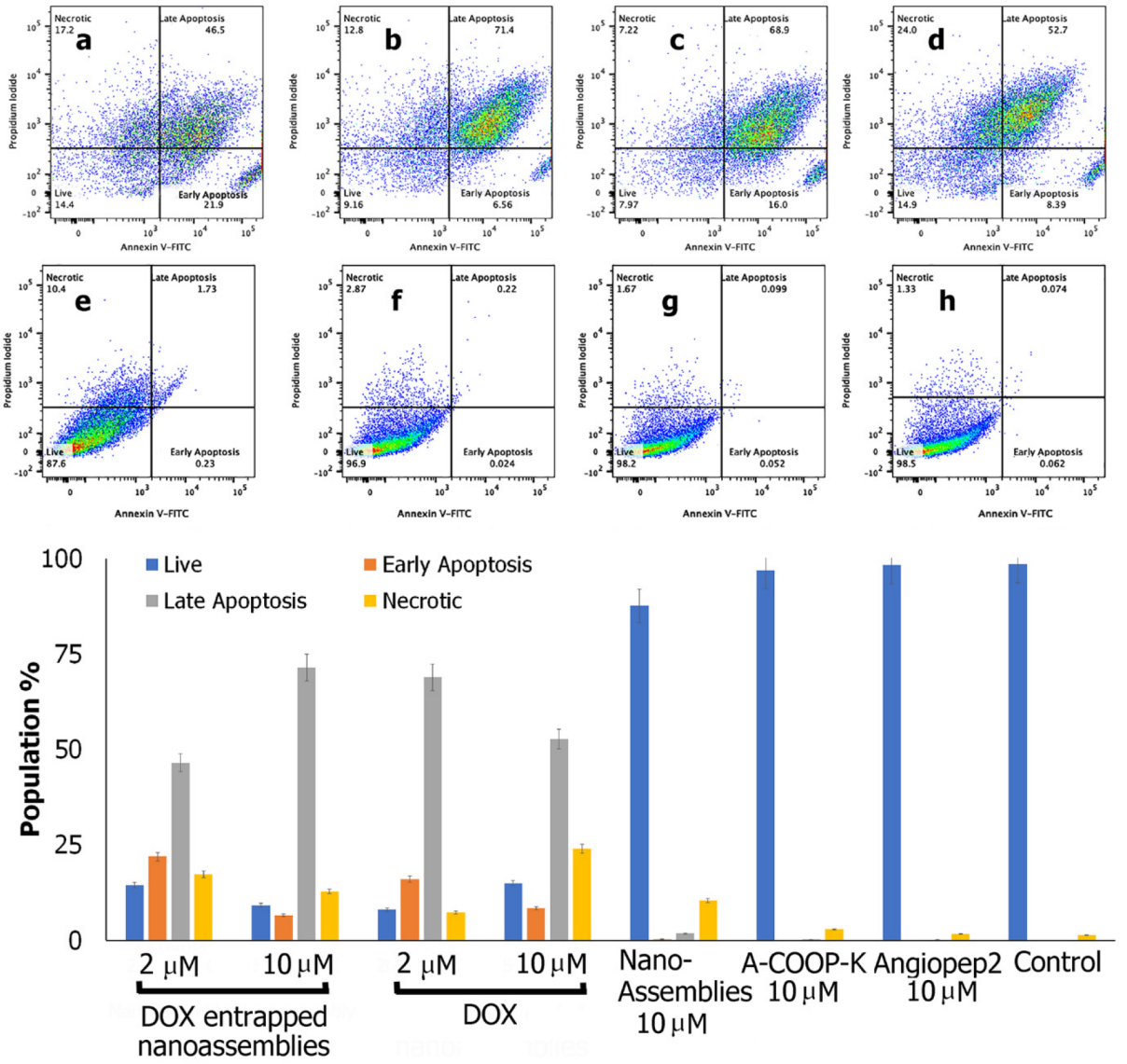

Figure 12. (a–h) Scatter plots obtained from FACS analysis showing the induction of apoptosis by various constructs. (a) DOX entrapped nanoassemblies (2 μM); (b) DOX entrapped nanoassemblies (10 μM); (c) DOX (2 μM); (d) DOX (10 μM); (e) nanoassemblies (neat, unentrapped with DOX); (f) angiopep-2 (10 μM); (g) A-COOP-K sequence (10 μM); (h) untreated cells. Bottom graph shows the quantitative analysis of various apoptotic, live, and necrotic cells upon treatment with various constructs.

Because the morphology of spheroids is dependent upon growth conditions such as cell density, culture media, mechanical stress,[116−119] it appears that the spheroids grown under serum-free conditions were found to be relatively less compact and formed less uniform aggregates of cells under the time frame studied. It may be plausible that over a longer period of time, tighter aggregates may form, leading to more spherical morphologies. The SEM images of the spheroids further confirm the multilayered structures obtained. A similar observation was seen for the spheroids grown with U-138 cells, where in more uniform spherical spheroids are seen for those grown in media supplemented with serum, while under serum-free conditions more wide, oblong shaped spheroids were obtained. These differences in morphologies may be indicative of different phenotypes which would imply differences in invasive behavior and reactivity upon drug treatment.[120]

3.8.2. Association and Internalization of DOX and DOX Entrapped Nanoassemblies into Spheroids. Spheroids grown for 7 days at a density of 10,000 cells/well were treated with DOX and DOX entrapped assemblies at concentration of 10 μM for 24 h. Spheroids grown in the presence and absence of serum were examined to determine the impact of the spheroid morphology and growth conditions on drug internalization. Fluorescence microscopy was utilized to analyze the effect of the drug entrapped nanoassemblies and neat DOX on the spheroids. As can be seen in Figure 14, overall higher penetration is observed for spheroids grown in neuronal basal media with B27 supplement (serum-free) in the case of DOX entrapped assemblies for both U-87 and U-138 spheroids. Dox alone also showed relatively higher penetration in spheroids grown in serum-free media compared with those grown in serum, though DOX appeared to be mainly accumulating in the periphery of the spheroids. Dox entrapped assemblies grown in serum showed a higher penetration in the case of U-87-MG spheroids compared to those seen for U-138 spheroids. Overall, the maximum fluorescence peak intensities

https://doi.org/10.1021/acsomega.2c08049
ACS Omega 2023, 8, 12124−12143

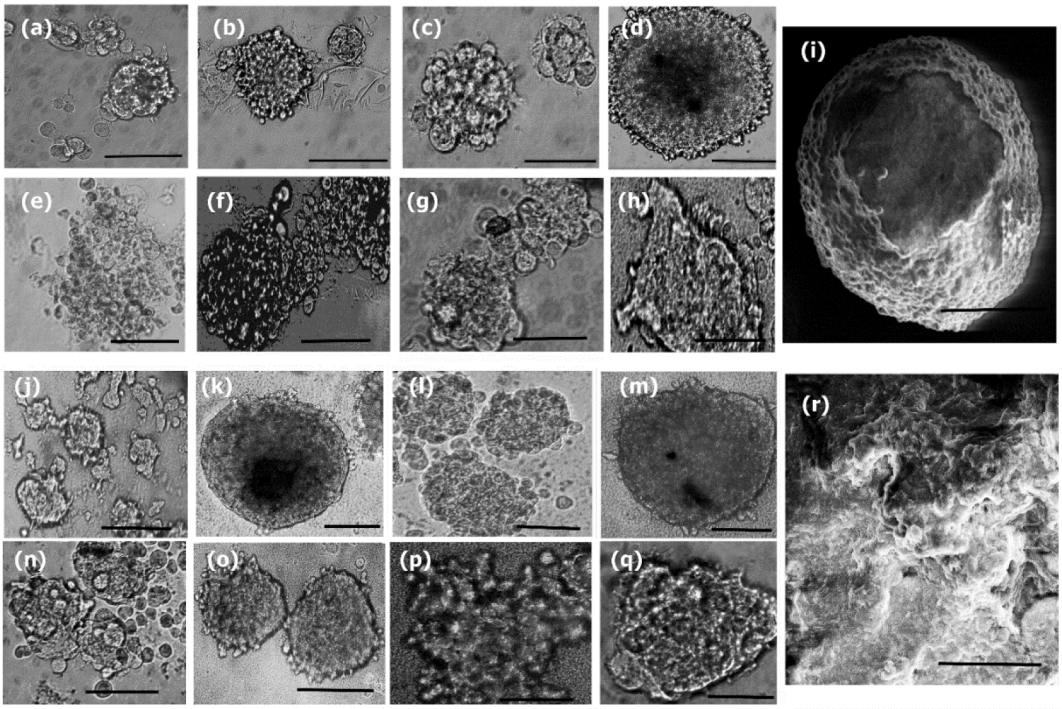

Figure 13. (a−d) Optical light microscopy images showing spheroid growth of U-87-MG cells grown in the presence of serum: (a,b) growth after 2 and 10 days, respectively, at a density of 4000 cells/well; (c,d) growth after 2 and 10 days, respectively, at a density of 10,000 cells/well. (e−h) Optical light microscopy images showing spheroid growth of U-87-MG cells grown in serum-free media: (e,f) growth after 2 and 10 days, respectively, at a density of 4000 cells/well; (g,h) growth after 2 and 10 days, respectively, at a density of 10,000 cells/well. Scale bar = 20 μM. (i) SEM micrograph of a single spheroid grown at 10,000 cell/well after 10 days of growth. Scale bar = 30 μM. (j−m) Optical light microscopy images showing spheroid growth of U-138-MG cells grown in the presence of serum: (j,k) growth after 2 and 10 days, respectively, at a density of 4000 cells/well; (l,m) growth after 2 and 10 days, respectively, at a density of 10,000 cells/well. (n−q) Optical light microscopy images showing spheroid growth of U-138-MG cells grown in serum-free media: (n,o) growth after 2 and 10 days, respectively, at a density of 4000 cells/well; (p,q) growth after 2 and 10 days, respectively, at a density of 10,000 cells/well. Scale bar = 20 μM. (r) SEM micrograph of a single spheroid grown at 10,000 cell/well after 10 days of growth. Scale bar = 30 μM.

were observed for DOX entrapped assemblies grown in serum-free media for U-87-MG spheroids followed closely by DOX. In comparison, a larger difference was observed for the U-138-MG spheroids grown in serum-free media, where the fluorescence was found to be significantly higher for DOX entrapped nanoassemblies compared to DOX indicating higher penetration and internalization of the assemblies toward the core. These results are corroborated with previous works where it has been shown that targeted drug delivery materials enhance penetration ability into spheroids.[107]

Thus, these results indicate that the aze5-angiopep-2-A-COOP-K nanoassemblies that had entrapped DOX showed relatively higher internalization, particularly for U-138 spheroids grown under serum-free conditions, which may be able to mimic *in vivo* tumoroids more closely.[121] These results imply that the nanoassemblies may have applications for future drug delivery to tumoroids. However, it is to be noted that these are single cell model spheroids, and further studies are being conducted where multicellular spheroids are being studied with these nanoassemblies.

3.8.3. Effects of DOX Entrapped Nanoassemblies on Spheroid Viability. To examine the effect of DOX entrapped nanoassemblies on the viability of the spheroids, Calcein-AM assay[122] was performed using six-day old spheroids grown with U-87-MG cells at 10000 cells/well. Results are shown in Figure 15. Calcein-AM is a lipophilic dye molecule that enters viable cells only when exposed to intracellular esterases leading to the formation of a green fluorochrome[123] and therefore can be utilized to explore the viability of spheroids upon drug treatment. As shown in Figure 15a untreated spheroids showed green fluorescence encompassing most of the spheroid except within parts of the interior which may have been necrotic.[124] Upon treatment with the DOX entrapped nanoassemblies (Figure 15b) the spheroids showed lesser viability, as indicated by lower fluorescence. While there were scattered areas, particularly around the edges that showed some viable cells, the majority of the spheroid did not show fluorescence. For the neat DOX-treated assemblies (Figure 15c), scattered viable cells were seen throughout the spheroid, indicating that it may be likely that slightly lesser DOX may have penetrated into the interior parts of the spheroid. However, the spheroid itself appeared to be disintegrating. This may be because the nanoassemblies release the drugs relatively slowly compared with neat DOX. Thus, the nanoassemblies entrapped with DOX may have been able to enter deeper into the spheroids and deliver the drug. These results indicate that such nanoassemblies may potentially be developed for the delivery of drugs to tumoroids.

4. CONCLUSIONS

In this work, we have developed new peptide-based nanoassemblies that are comprised of three components, namely azelaic acid, angiopep-2 and A-COOP-K. The nanoassemblies were designed to target U-87 and U-138-MG tumor cells as models for glioblastoma tumor cells in vitro. The expression of endogenous LRP1 and FABP3 receptors by these cells grown

https://doi.org/10.1021/acsomega.2c08049
ACS Omega 2023, 8, 12124−12143

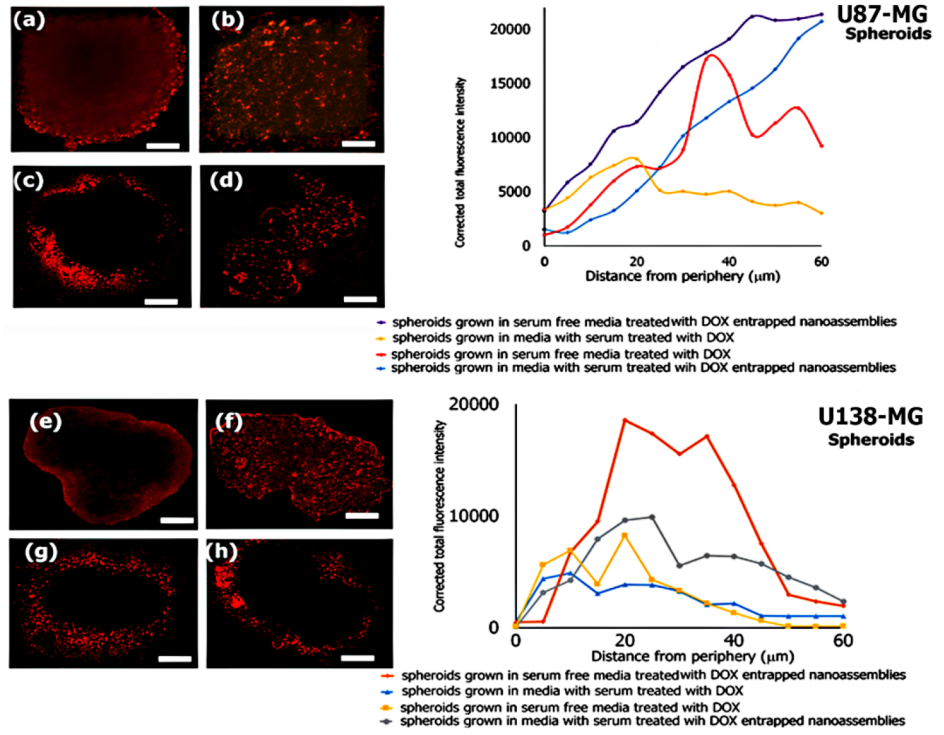

Figure 14. Top: Fluorescence micrographs of U-87 spheroids: (a) grown in the presence of serum and treated with DOX entrapped nanoassemblies; (b) grown in the absence of serum and treated with DOX entrapped nanoassemblies; (c) grown in the presence of serum and treated with DOX; (d) grown in the absence of serum and treated with DOX. Scale bar = 20 μm. Top right shows the corrected DOX fluorescence intensity representing the association of DOX entrapped nanoassemblies and DOX in U-87 spheroids from the periphery to inner core. Bottom: Fluorescence micrographs of U-138 spheroids: (e) grown in the presence of serum and treated with DOX entrapped nanoassemblies; (f) grown in the absence of serum and treated with DOX entrapped nanoassemblies; (g) grown in the presence of serum and treated with DOX; (h) grown in the absence of serum and treated with DOX. Scale bar = 20 μm. Bottom right shows the corrected DOX fluorescence intensity representing the association of DOX entrapped nanoassemblies and DOX in U-138 spheroids from the periphery to inner core.

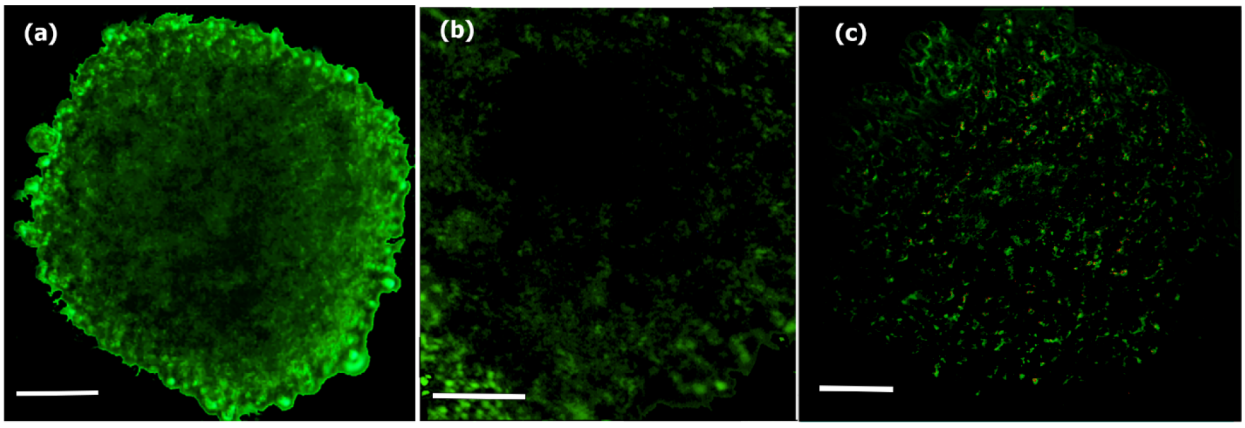

Figure 15. Fluorescence images of six-day old spheroids grown with U-87-MG cells after calcein staining: (a) untreated spheroids; (b) spheroids treated with DOX loaded nanoassemblies at 10 μM concentration; (c) neat DOX-treated spheroids at 10 μM concentration. Scale bar: 20 μm.

in the presence and absence of serum was examined and it was found that higher LRP1 expression was observed for U-87-MG cells compared to U-138 cells in serum-free conditions. FABP3 expression was found to be low in both cases. FACS analysis revealed that the nanoassemblies demonstrated LRP1-mediated internalization for both cell lines, while FABP3-mediated internalization was found to be negligible. Furthermore, the nanoassemblies showed BBB penetration when tested with an in vitro multicellular cocultured BBB model. The assemblies were found to form nanofibrous hierarchical structures that were able to successfully entrap the drug doxorubicin. Drug release studies showed a concentration dependent release with a burst release seen at the higher concentration followed by a stepwise release over a longer period of time. The drug entrapped nanoassemblies resulted in lower cell proliferation in a concentration-dependent manner similar to that of DOX. Both 2D cultured cells and spheroids grown in the presence and absence of serum were tested. The induction of apoptosis was confirmed by FACS analysis for the U-87-MG cells as a proof of concept. 3D spheroids were constructed at different cell densities grown in the presence and absence of serum to create models that mimic tumoroids. The internalization of

https://doi.org/10.1021/acsomega.2c08049
ACS Omega 2023, 8, 12124−12143

DOX and DOX entrapped nanoassemblies indicated higher penetration into the core for the DOX entrapped assemblies, particularly for U-138 spheroids grown under serum-free conditions. The morphologies were found to be well-rounded and spherical in the presence of serum, whereas less symmetrical, larger aggregated structures were seen for those grown under serum-free conditions. Thus, these nanoassemblies may provide insights into drug-biomaterial interactions and can be further developed for exploring multicellular tumoroids. Furthermore, they may potentially enhance internalization and targeting of glioblastoma cells.

■ ASSOCIATED CONTENT

Supporting Information

The Supporting Information is available free of charge at https://pubs.acs.org/doi/10.1021/acsomega.2c08049.

Comparison of FTIR spectra of angiopep-2, A-COOP-K peptides with Aze5-angiopep-2 nanoassemblies and Aze5-angiopep-2-A-COOP-K bound assemblies (PDF)

■ AUTHOR INFORMATION

Corresponding Author

Ipsita A. Banerjee − *Department of Chemistry, Fordham University, Bronx, New York 10458, United States;* orcid.org/0000-0002-6987-9717; Email: banerjee@fordham.edu

Authors

Charlotta G. Lebedenko − *Department of Chemistry, Fordham University, Bronx, New York 10458, United States*

Molly E. Murray − *Department of Chemistry, Fordham University, Bronx, New York 10458, United States*

Beatriz G. Goncalves − *Department of Chemistry, Fordham University, Bronx, New York 10458, United States*

Diego S. Perez − *Department of Chemistry, Fordham University, Bronx, New York 10458, United States*

Dominic J. Lambo − *Department of Chemistry, Fordham University, Bronx, New York 10458, United States*

Complete contact information is available at: https://pubs.acs.org/10.1021/acsomega.2c08049

Author Contributions

C.G.L., M.E.M., and B.G.G. contributed equally to this work. C.G.L. and D.S.P. were responsible for initial synthesis of the nanoassemblies and characterization. C.G.L. wrote parts of the introduction. D.J.L. conducted AFM imaging. M.E.M. and B.G.G. conducted all in vitro experiments (both 2D and 3D) and also helped with data analysis and writing parts of the manuscript. I.A.B. was responsible for conception, supervision, data analysis and writing the final manuscript.

Notes

The authors declare no competing financial interest.

■ ACKNOWLEDGMENTS

I.A.B. thanks NSF MRI Grant No. 1626378 and NSF MRI Grant No. 2117625 for the acquisition of the AFM and FACS instruments respectively. C.G.L., D.S.P., D.J.L., and I.A.B. thank Fordham University research grants for financial support of this work. M.E.M. and B.G.G. thank the Clare Boothe Luce Foundation and Fordham University Research Grants for financial support of this work.

■ ABBREVIATIONS

Aze:azelaic acid; angiopep-2:TFFYGGSRGKRNNFKTEEY; A-COOP-K:ACGLSGLCVAK sequence

■ REFERENCES

(1) Stefanick, J. F.; Omstead, D. T.; Kiziltepe, T.; Bilgicer, B. Dual-receptor targeted strategy in nanoparticle design achieves tumor cell selectivity through cooperativity. *Nanoscale* **2019**, *11*, 4414−4427.

(2) Sharma, P.; Sonawane, P.; Herpai, D.; D'Agostino, R.; Rossmeisl, J.; Tatter, S.; Debinski, W. Multireceptor targeting of glioblastoma. *Neuro-Oncol. Adv.* **2020**, *2*, vdaa107.

(3) Hanif, F.; Muzaffar, K.; Malhi, S. M.; Perveen, K.; Simjee, S. U. Glioblastoma Multiforme: A Review of Its Epidemiology and Pathogenesis through Clinical Presentation and Treatment. *Asian Pac J. Cancer Prev* **2017**, *18*, 3−9.

(4) Sharma, P.; Debinski, W. Receptor-Targeted Glial Brain Tumor Therapies. *Int. J. Mol. Sci.* **2018**, *19*, 3326.

(5) Ware, M. L.; Berger, M. S.; Binder, D. K. Molecular Biology of Glioma Tumorigenesis. *Histol. Histopathol.* **2003**, *18*, 207−16.

(6) Olar, A.; Aldape, K. D Using the Molecular Classification of Glioblastoma to Inform Personalized Treatment. *J. Pathol.* **2014**, *232*, 165−77.

(7) Jung, T.-Y.; Choi, Y.-D.; Kim, Y.-H.; Lee, J.-J.; Kim, H.-S.; Kim, J.-S.; Kim, S.-K.; Jung, S.; Cho, D. Immunological Characterization of Glioblastoma Cells for Immunotherapy. *Anticancer Res.* **2013**, *33*, 2525−2533.

(8) Bhaskaran, M.; Devegowda, V. G.; Gupta, V. K.; Shivachar, A.; Bhosale, R. R.; Arunachalam, M.; Vaishnavi, T. Current Perspectives on Therapies, Including Drug Delivery Systems, for Managing Glioblastoma Multiforme. *ACS Chem. Neurosci.* **2020**, *11*, 2962−77.

(9) Skinner, M.; Ward, S. M.; Nilsson, C. L.; Emrick, T. Augmenting Glioblastoma Chemotherapy with Polymers. *ACS Chem. Neurosci* **2018**, *9*, 8−10.

(10) Delehanty, J. B.; Boeneman, K.; Bradburne, C. E.; Robertson, K.; Bongard, J. E.; Medintz, I. L. Peptides for Specific Intracellular Delivery and Targeting of Nanoparticles: Implications for Developing Nanoparticle-Mediated Drug Delivery. *Ther Deliv* **2010**, *1*, 411−33.

(11) Bertrand, Y.; Currie, J.-C.; Demeule, M.; Régina, A.; Ché, C.; Abulrob, A.; Fatehi, D.; Sartelet, H.; Gabathuler, R.; Castaigne, J.-P.; Stanimirovic, D.; Béliveau, R. Transport Characteristics of a Novel Peptide Platform for CNS Therapeutics. *J. Cell. Mol. Med.* **2010**, *14*, 2827−39.

(12) Stalmans, S.; Bracke, N.; Wynendaele, E.; Gevaert, B.; Peremans, K.; Burvenich, C.; Polis, I.; De Spiegeleer, B. Cell-Penetrating Peptides Selectively Cross the Blood-Brain Barrier In Vivo. *PLoS One* **2015**, *10*, e0139652.

(13) Baranyai, Z.; Biri-Kovács, B.; Krátký, M.; Szeder, B.; Debreczeni, M. L.; Budai, J.; Kovács, B.; Horváth, L.; Pári, E.; Nemeth, Z.; Cervenak, L.; Zsila, F.; Mehes, E.; Kiss, E.; Vinsová, J.; Bosze, S. Cellular Internalization and Inhibition Capacity of New Anti-Glioma Peptide Conjugates: Physicochemical Characterization and Evaluation on Various Monolayer- and 3D-Spheroid-Based in Vitro Platforms. *J. Med. Chem.* **2021**, *64*, 2982−3005.

(14) Ayo, A.; Laakkonen, P. Peptide-Based Stratagies for Targeted Tumor Treatment and Imaging. *Pharmaceutics* **2021**, *13*, 481.

(15) Bock, T.; Moest, H.; Omasits, U.; Dolski, S.; Lundberg, E.; Frei, A.; Hofmann, A.; Bausch-Fluck, D.; Jacobs, A.; Krayenbuehl, N.; Uhlen, M.; Aebersold, R.; Frei, K.; Wollscheid, B. Proteomic Analysis Reveals Drug Accessible Cell Surface N-Glycoproteins of Primary and Established Glioblastoma Cell Lines. *J. Proteome Res.* **2012**, *11*, 4885−93.

(16) Zhang, L.; Shan, X.; Meng, X.; Gu, T.; Guo, L.; An, X.; Jiang, Q.; Ge, H.; Ning, X. Novel Integrin Avβ3-Specific Ligand for the Sensitive Diagnosis of Glioblastoma. *Mol. Pharmaceutics* **2019**, *16*, 3977−84.

(17) Agemy, L.; Friedmann-Morvinski, D.; Kotamraju, V. R.; Roth, L.; Sugahara, K. N.; Girard, O. M.; Mattrey, R. F.; Verma, I. M.; Ruoslahti, E. Targeted Nanoparticle Enhanced Proapoptotic Peptide

as Potential Therapy for Glioblastoma. *Proc. Natl. Acad. Sci. U.S.A.* **2011**, *108*, 17450−55.
(18) Zhai, M.; Wang, Y.; Zhang, L.; Liang, M.; Fu, S.; Cui, L.; Yang, M.; Gong, W.; Li, Z.; Yu, L.; Xie, X.; Yang, C.; Yang, Y.; Gao, C. Glioma Targeting Peptide Modified Apoferritin Nanocage. *Drug Delivery* **2018**, *25* (1), 1013−24.
(19) Li, Y.; Zhang, J.; Zheng, X.; Gong, M. Delivery of a Peptide-Drug Conjugate Targeting the Blood Brain Barrier Improved the Efficacy of Paclitaxel against Glioma. *Oncotarget* **2016**, *7*, 79401−79407.
(20) Yan, H.; Wang, L.; Wang, J.; Weng, X.; Lei, H.; Wang, X.; Jiang, L.; Zhu, J.; Lu, W.; Wei, X.; Li, C. Two-Order Targeted Brain Tumor Imaging by Using an Optical/Paramagnetic Nanoprobe across the Blood Brain Barrier. *ACS Nano* **2012**, *6*, 410−20.
(21) Wang, Z.; Zhou, X.; Xu, Y.; Fan, S.; Tian, N.; Zhang, W.; Sheng, F.; Lin, J.; Zhong, W. Development of a Novel Dual-Order Protein-Based Nanodelivery Carrier That Rapidly Targets Low-Grade Gliomas with Microscopic Metastasis in Vivo. *ACS Omega* **2020**, *5*, 20653−63.
(22) Chen, L.; Xu, N.; Li, C.; Zhang, W.; Zhu, X.; Chen, P. R.; Lin, J.; Zeng, D.; Gao, Y. Blood-Brain Barrier- And Blood-Brain Tumor Barrier-Penetrating Peptide-Derived Targeted Therapeutics for Glioma and Malignant Tumor Brain Metastases. *ACS Appl. Mater. Interfaces* **2019**, *11*, 41889−97.
(23) Singh, A. V.; Chandrasekar, V.; Janapareddy, P.; Mathews, D. E.; Laux, P.; Luch, A.; Yang, Y.; Garcia-Canibano, B.; Balakrishnan, S.; Abinahed, J.; Al Ansari, A.; Dakua, S. P. Emerging Application of Nanorobotics and Artificial Intelligence to Cross the BBB: Advances in Design, Controlled Maneuvering, and Targeting of the Barriers. *ACS Chem. Neurosci.* **2021**, *12*, 1835−53.
(24) Tan, S. K.; Jermakowicz, A.; Mookhtiar, A. K.; Nemeroff, C. B.; Schürer, S. C.; Ayad, N. G. Drug Repositioning in Glioblastoma: A Pathway Perspective. *Front Pharmacol* **2018**, *9*, 218.
(25) Banerjee, S.; Bhat, M. A. Neuron-Glial Interactions in Blood-Brain Barrier Formation. *Annu. Rev. Neurosci.* **2007**, *30*, 235−58.
(26) Sivasubramanian, M.; Hsia, Y.; Lo, L.-W. Nanoparticle-Facilitated Functional and Molecular Imaging for the Early Detection of Cancer. *Front. Mol. Biosci.* **2014**, *1*, 15.
(27) Saalik, P.; Lingasamy, P.; Toome, K.; Mastandrea, I.; Rousso-Noori, L.; Tobi, A.; Simon-Gracia, L.; Hunt, H.; Paiste, P.; Kotamraju, V. R.; Bergers, G.; Asser, T.; Ratsep, T.; Ruoslahti, E.; Bjerkvig, R.; Friedmann-Morvinski, D.; Teesalu, T. Peptide-guided nanoparticles for glioblastoma targeting. *J. Controlled Release* **2019**, *308*, 109−118.
(28) Zhang, B.; Shen, S.; Liao, Z.; Shi, W.; Wang, Y.; Zhao, J.; Hu, Y.; Yang, J.; Chen, J.; Mei, H.; Hu, Y.; Pang, Z.; Jiang, X. Targeting fibronectins of glioma extracellular matrix by CLT1 peptide-conjugated particles. *Biomaterials.* **2014**, *35*, 4088−4098.
(29) Chen, J.; Jiang, Z.; Zhang, Y. S.; Ding, J.; Chen, X. Smart transformable nanoparticle for enhanced tumor theranostics. *Appl. Phys. Rev.* **2021**, *8*, 041321.
(30) Ding, J.; Chen, J.; Gao, L.; Jiang, Z.; Zhang, Y.; Li, M.; Xiao, Q.; Lee, S.; Chen, X. Engineered nanomedicines with enhanced tumor penetration. *Nano Today* **2019**, *29*, 100800.
(31) Demeule, M.; Regina, A.; Poirier, J.; Béliveau, R.; Ché, C.; Nguyen, T.; Gabathuler, R.; Castaigne, J.-P. Identification and Design of Peptides as a New Drug Delivery System for the Brain. *J. Pharm. Exp. Therap.* **2008**, *324*, 1064−72.
(32) Yamamoto, M.; Ikeda, K.; Ohshima, K.; Tsugu, H.; Kimura, H.; Tomonaga, M. Increased Expression of Low Density Lipoprotein Receptor-Related Protein/Alpha2-Macroglobulin Receptor in Human Malignant Astrocytomas. *Cancer Res.* **1997**, *57*, 2799−2805.
(33) Gonias, S. L.; Campana, W. M. LDL receptor−related protein-1: a regulator of inflammation in atherosclerosis, cancer, and injury to the nervous system. *Am. J. Pathol.* **2014**, *184*, 18−27.
(34) Spuch, C.; Ortolano, S.; Navarro, C. LRP-1 and LRP-2 Receptors Function in the Membrane Neuron. Trafficking Mechanisms and Proteolytic Processing in Alzheimer's Disease. *Front. Phys.* **2012**, *3*, 269.
(35) Maletínská, L.; Blakely, E. A.; Bjornstad, K. A.; Knoff, L. J.; Forte, T. M.; Deen, D. F. Human Glioblastoma Cell Lines: Levels of Low-Density Lipoprotein Receptor and Low-Density Lipoprotein Receptor-Related Protein. *Cancer Res.* **2000**, *60*, 2300−2303.
(36) Song, H.; Lee, J.; Schwartz, A. L.; Bu, G.; Li, Y. 2009. Low-Density Lipoprotein Receptor-Related Protein 1 Promotes Cancer Cell Migration and Invasion by Inducing the Expression of Matrix Metalloproteinases 2 and 9. *Cancer Res.* **2009**, *69*, 879−86.
(37) Pucci, C.; De Pasquale, D.; Marino, A.; Martinelli, C.; Ciofani, G.; Lauciello, S. Hybrid Magnetic Nanovectors Promote Selective Glioblastoma Cell Death through a Combined Effect of Lysosomal Membrane Permeabilization and Chemotherapy. *ACS Appl. Mater. Interfaces* **2020**, *12*, 29037−29055.
(38) Demeule, M.; Currie, J.-C.; Bertrand, Y.; Ché, C.; Nguyen, T.; Régina, A.; Gabathuler, R.; Castaigne, J.-P.; Béliveau, R. Involvement of the Low-Density Lipoprotein Receptor-Related Protein in the Transcytosis of the Brain Delivery Vector Angiopep-2. *J. Neurochem.* **2008**, *106*, 1534−44.
(39) Ché, C.; Yang, G.; Thiot, C.; Lacoste, M.-C.; Demeule, M.; Régina, A.; Castaigne, J.-P.; Currie, J.-C.; Béliveau, R. New Angiopep-Modified Doxorubicin (ANG1007) and Etoposide (ANG1009) Chemotherapeutics with Increased Brain Penetration. *J. Med. Chem.* **2010**, *53*, 2814−24.
(40) Bertrand, Y.; Currie, J.-C.; Poirier, J.; Demeule, M.; Abulrob, A.; Fatehi, D.; Stanimirovic, D.; Sartelet, H.; Castaigne, J.-P.; Béliveau, R. Influence of Glioma Tumor Microenvironment on the Transport of ANG1005 via Low-Density Lipoprotein Receptor-Related Protein 1. *Br. J. Cancer.* **2011**, *105*, 1697−1707.
(41) He, C.; Zhang, Z.; Ding, Y.; Xue, K.; Wang, K.; Yang, R.; An, Y.; Liu, D.; Hu, C.; Tang, Q. LRP1-Mediated PH-Sensitive Polymersomes Facilitate Combination Therapy of Glioblastoma in Vitro and in Vivo. *J. Nanobiotech.* **2021**, *19*, 29.
(42) Régina, A.; Demeule, M.; Ché, C.; Lavallée, I.; Poirier, J.; Gabathuler, R.; Béliveau, R.; Castaigne, J. P. Antitumour activity of ANG1005, a conjugate between paclitaxel and the new brain delivery vector Angiopep-2. *Br. J. Pharmacol.* **2008**, *155*, 185−97.
(43) Xin, H.; Sha, X.; Jiang, X.; Zhang, W.; Chen, L.; Fang, X. Anti-Glioblastoma Efficacy and Safety of Paclitaxel-Loading Angiopep-Conjugated Dual Targeting PEG-PCL Nanoparticles. *Biomaterials* **2012**, *33*, 8167−76.
(44) Lu, F.; Pang, Z.; Zhao, J.; Jin, K.; Li, H.; Pang, Q.; Zhang, L.; Pang, Z. Angiopep-2-Conjugated Poly(Ethylene Glycol)-Co-Poly(ε-Caprolactone) Polymersomes for Dual-Targeting Drug Delivery to Glioma in Rats. *Int. J. Nanomed.* **2017**, *12*, 2117−27.
(45) Shao, K.; Wu, J.; Chen, Z.; Huang, S.; Li, J.; Ye, L.; Lou, J.; Zhu, L.; Jiang, C. A brain-vectored angiopep-2 based polymeric micelles for the treatment of intracranial fungal infection. *Biomaterials* **2012**, *33*, 6898−6907.
(46) Tapia-Arellano, A.; Gallardo-Toledo, E.; Ortiz, C.; Henriquez, J.; Feijoo, C. G.; Araya, E.; Sierpe, R.; Kogan, M. J. Functionalization with PEG/Angiopep-2 peptide to improve the delivery of gold nanoprisms to central nervous system: in vitro and in vivo studies. *Mater. Sci. Eng., C* **2021**, *121*, 111785.
(47) Seano, G.; Jain, R. K. Vessel co-option in glioblastoma: emerging insights and opportunities. *Angiogenesis* **2020**, *23*, 9−16.
(48) Lewis, C. A.; Brault, C.; Peck, B.; Bensaad, K.; Griffiths, B.; Mitter, R.; Chakravarty, P.; East, P.; Dankworth, B.; Alibhai, D.; Harris, A. L.; Schulze, A. SREBP maintains lipid biosynthesis and viability of cancer cells under lipid- and oxygen-deprived conditions and defines a gene signature associated with poor survival in glioblastoma multiforme. *Oncogene.* **2015**, *34*, 5128−40.
(49) Falomir-Lockhart, L. J.; Cavazzutti, G. F.; Giménez, E.; Toscani, A. M. Fatty acid signaling mechanisms in neural cells: fatty acid receptors. *Front. Cell. Neur.* **2019**, *13*, 162.
(50) Elmes, M. W.; Kaczocha, M.; Berger, W. T.; Leung, K.; Ralph, B. P.; Wang, L.; Sweeney, J. M.; Miyauchi, J. T.; Tsirka, S. E.; Ojima, I.; Deutsch, D. G. Fatty Acid-Binding Proteins (FABPs) Are Intracellular Carriers for Δ9-Tetrahydrocannabinol (THC) and Cannabidiol (CBD). *J. Bio. Chem.* **2015**, *290*, 8711−21.

https://doi.org/10.1021/acsomega.2c08049
ACS Omega 2023, 8, 12124−12143

(51) Le Joncour, V.; Filppu, P.; Hyvonen, M.; Holopainen, M.; Turunen, S P.; Sihto, H.; Burghardt, I.; Joensuu, H.; Tynninen, O.; Jaaskelainen, J.; Weller, M.; Lehti, K.; Kakela, R.; Laakkonen, P. Vulnerability of Invasive Glioblastoma Cells to Lysosomal Membrane Destabilization. *EMBO Mol. Med.* **2019**, *11*, e9034.
(52) Hyvonen, M.; Enback, J.; Huhtala, T.; Lammi, J.; Sihto, H.; Weisell, J.; Joensuu, H.; Rosenthal-Aizman, K.; El-Andaloussi, S.; Langel, U.; Närvänen, A.; Bergers, G.; Laakkonen, P. Novel target for peptide-based imaging and treatment of brain tumors. *Mol. Cancer Ther.* **2014**, *13*, 996−1007.
(53) Ayo, A.; Laakkonen, P.; Figueras, E.; Schachtsiek, T.; Budak, M.; Sewald, N. Tumor-Targeting Peptides: The Functional Screen of Glioblastoma Homing Peptides to the Target Protein FABP3 (MDGI). *Cancers* **2020**, *12*, 1836.
(54) Kinnari, P. J.; Hyvönen, M. K.; Mäkilä, E. M.; Kaasalainen, M. H.; Rivinoja, A.; Salonen, J. J.; Hirvonen, J. T.; Laakkonen, P. M.; Santos, H. A. Tumour Homing Peptide-Functionalized Porous Silicon Nanovectors for Cancer Therapy. *Biomaterials* **2013**, *34*, 9134−9141.
(55) Feng, X.; Kang, T.; Jiang, D.; Yao, J.; Jing, Y.; Jiang, X.; Liang, J.; Chen, J.; Gao, X.; Song, Q. Mammary-Derived Growth Inhibitor Targeting Peptide-Modified PEG-PLA Nanoparticles for Enhanced Targeted Glioblastoma Therapy. *Bioconj. Chem.* **2015**, *26*, 1850−1861.
(56) Daso, R. E.; Osborn, L. J.; Thomas, M. F.; Banerjee, I. A. Development of nanoscale hybrids from ionic liquid-peptide amphiphile assemblies as new functional materials. *ACS Omega* **2020**, *5*, 14543−14554.
(57) Menzenski, M. Z.; Banerjee, I. A. Self-assembly of supramolecular nanostructures from phenylalanine derived bolaamphiphiles. *New J. Chem.* **2007**, *31*, 1674−1680.
(58) Pan, Y.; Liu, D.; Wei, Y.; Su, D.; Lu, C.; Hu, Y.; Zhou, F. Azelaic acid exerts antileukemic activity in acute myeloid leukemia. *Front. Pharmacol.* **2017**, *8*, 359.
(59) Zaffaroni, N.; Villa, R.; Silverstro, L.; Sanfilippo, O.; Silvestrini, R. Cytotoxic activity of azelaic acid against human melanoma primary cultures and established cell lines. *Anticancer Res.* **1990**, *10*, 1599−1602.
(60) Farias, C. B.; Lima, R. C.; Lima, L. O.; Flores, D. G.; Meurer, L.; Brunetto, A. L.; Schwartsmann, G.; Roesler, R. Stimulation of proliferation of U138-MG glioblastoma cells by gastrin-releasing peptide in combination with agents that enhance cAMP signaling. *Oncology* **2008**, *75*, 27−31.
(61) Pokorna, M.; Hudec, M.; Jurickova, I.; Vacha, M.; Polivkova, Z.; Kutna, V.; Pala, J.; Ovsepian, S. V.; Cerna, M.; O'Leary, V. B. All-tran retinoic acid fosters the multifarious U-87MG cell line as a model of glioblastoma. *Brain Sci.* **2021**, *11*, 812.
(62) Ricci-Vitiani, L.; Lombardi, D. G.; Pilozzi, E.; Biffoni, M.; Todaro, M.; Peschle, C.; De Maria, R. Identification and expansion of human colon-cancer-initiating cells. *Nature* **2007**, *445*, 111−115.
(63) Vik-Mo, E.; Sandberg, C.; Olstorn, H.; Varghese, M.; Brandal, P.; Ramm-Pettersen, J.; Murrell, W.; Langmoen, I. A. Brain tumor stem cells maintain overall phenotype and tumorigeicity after in vitro culturing in serum free conditions. *Neuro Oncol.* **2010**, *12*, 1220−1230.
(64) Yan, Q.; Zheng, H.-N.; Jiang, C.; Li, K.; Xiao, S.-J. EDC/NHS activation mechanism of polymethacrylic acid: anhydride versus NHS-ester. *RSC Adv.* **2015**, *5*, 69939−69947.
(65) Chiang, L.-C.; Silnutzer, J.; Pipas, J. M.; Barnes, D. W. Selection of transformed cells in serum-free media. *In Vitro Cell. Dev. Biol.* **1985**, *21*, 707−712.
(66) Plumb, J. A. Cell Sensitivity Assays: *The MTT Assay*. In *Methods in Molecular Medicine*; Langdon, S. P., Ed. Cancer Cell Culture; Humana Press, 2004, Vol. *88*.
(67) Tung, J.; Parks, D. R.; Moore, W. A.; Herzenberg, L. A.; Herzenberg, L. A. New approaches to fluorescence compensation and visualization of FACS data. *Clin. Immunol.* **2004**, *110*, 277−283.
(68) Deleyrolle, L. P.; Harding, A.; Cato, K.; Siebzehnrubl, F. A.; Rahman, M.; Azari, H.; Olson, S.; Gabrielli, B.; Osborne, G.; Vescovi, A.; Reynolds, B. A. Evidence for label-retaining tumour-initiating cells in human glioblastoma. *Brain* **2011**, *134*, 1331−1343.
(69) Williams-Medina, A.; Deblock, M.; Janigro, D. In vitro models of the blood-brain barrier: Tools in translational medicine. *Front. Med. Technol.* **2021**, *2*, 623950.
(70) Fu, B. M.; Zhao, Z.; Zhu, D. Blood-Brain Barrier (BBB) Permeability and Transport Measurement In Vitro and In Vivo. *Methods Mol. Biol.* **2020**, *2367*, 105−122.
(71) GraphPad Prism (RRID:SCR_002798).
(72) Maritan, S. M.; Lian, E. Y.; Mulligan, L. M. An Efficient and Flexible Cell Aggregation Method for 3D Spheroid Production. *J. Vis. Exp.* **2017**, *121*, 55544.
(73) Schneider, C. A.; Rasband, W. S.; Eliceiri, K. W. NIH Image to ImageJ: 25 years of image analysis. *Nat. Methods* **2012**, *9*, 671−675.
(74) Achilli, T.-M.; McCalla, S.; Meyer, J.; Tripathi, A.; Morgan, J. R. Multilayer spheroids to quantify drug uptake and diffusion in 3D. *Mol. Pharmaceutics.* **2014**, *11*, 2071−2081.
(75) Sergent-Tanguy, S.; Chagneau, C.; Neveu, I.; Naveilhan, P. Fluorescent activated cell sorting (FACS): a rapid and reliable method to estimate the number of neurons in a mixed population. *J. Neurosci. Methods* **2003**, *129*, 73−79.
(76) Stendahl, J. C.; Rao, M. S.; Guler, M. O.; Stupp, S. I. Intermolecular Forces in the Self-Assembly of Peptide Amphiphile Nanofibers. *Adv. Funct. Mater.* **2006**, *16*, 499−508.
(77) Hunter, C. A.; Singh, J.; Thornton, J. M. π-π interactions: The geometry and energetics of phenylalanine-phenylalanine interactions in proteins. *J. Mol. Biol.* **1991**, *218*, 837−846.
(78) Szaraz, I.; Forsling, W. Spectroscopic Study of the Simultaneous Adsorption of PVP and Azelaic Acid on γ-Alumina. *Langmuir* **2001**, *17*, 3987−3996.
(79) Zong, Z.; Hua, L.; Wang, Z.; Xu, H.; Ye, C.; Pan, B.; Zhao, Z.; Zhang, L.; Lu, J.; Liu, H.; Yu, R. Self-assembled angiopep-2 modified lipid-poly (hypoxic radiosensitized polyprodrug) nanoparticles delivery TMS for glioma synergistic TMZ and RT therapy. *Drug Del.* **2019**, *26*, 34−44.
(80) Han, S.; Zheng, H.; Lu, Y.; Sun, Y.; Huang, A.; Fei, W.; Shi, X.; Xu, X.; Li, J.; Li, F. A novel synergetic targeting strategy for glioma therapy employing borneol combination with angiopep-2-modified, DOX-loaded PAMAM dendrimer. *J. Drug Target* **2018**, *26*, 86−94.
(81) Parrasia, S.; Rossa, A.; Varanita, T.; Checchetto, V.; De Lorenzi, R.; Zoratti, M.; Paradisi, C.; Ruzza, P.; Mattarei, A.; Szabò, I.; Biasutto, L. An Angiopep2-PAPTP Construct Overcomes the Blood-Brain Barrier. New Perspectives against Brain Tumors. *Pharmaceuticals* **2021**, *14*, 129.
(82) Brahms, S.; Brahms, J.; Spach, G.; Brack, A. Identification of β,β-turns and unordered conformations in polypeptide chains by vacuum ultraviolet circular dichroism. *Proc. Natl. Acad. Sci. U. S. A.* **1977**, *74*, 3208−3212.
(83) Han, S.; Cao, S.; Wang, Y.; Wang, J.; Xia, D.; Xu, H.; Zhao, X.; Lu, J. R. Self-assembly of Short Peptide Amphiphiles: The Cooperative Effect of Hydrophobic Interaction and Hydrogen Bonding. *Chem.—Eur. J.* **2011**, *17*, 13095−13102.
(84) Shu, C.; Li, T.; Yang, W.; Li, D.; Ji, S.; Ding, L. Amphotericin B-conjugated polypeptide hydrogels as a novel innovative strategy for fungal infections. *R. Soc. Open Sci.* **2018**, *5*, 171814.
(85) Kong, J.; Yu, S. Fourier Transform Infrared Spectroscopic Analysis of Protein Secondary Structures. *Acta Biochimica Biophysica Sinica* **2007**, *39*, 549−559.
(86) Goormaghtigh, E.; Cabiaux, V.; Ruysschaert, J. M. Determination of Soluble and Membrane Protein Structure by Fourier Transform Infrared Spectroscopy. *Subcell. Biochem.* **1994**, *23*, 405−450.
(87) Israel, L. L.; Braubach, O.; Galstyan, A.; Chiechi, A.; Shatalova, E. S.; Grodzinski, Z.; Ding, H.; Black, K. L.; Ljubimova, J. Y.; Holler, E. A Combination of Tri-Leucine and Angiopep-2 Drives a Poly-Anionic Polymalic Acid Nanodrug Platform Across the Blood-Brain Barrier. *ACS Nano* **2019**, *13*, 1253−1271.
(88) Bansal, R.; Singh, R.; Kaur, K. Quantitative analysis of doxorubicin hydrochloride and arterolane maleate by mid IR

https://doi.org/10.1021/acsomega.2c08049
ACS Omega 2023, 8, 12124−12143

spectroscopy using transmission and reflectance modes. *BMC Chem.* **2021**, *15*, 27.
(89) Kanwal, U.; Bukhari, N. I.; Rana, N. F.; Rehman, M.; Hussain, K.; Abbas, N.; Mehmood, A.; Raza, A. Doxorubicin-loaded quaternary ammonium palmitoyl glycol chitosan polymeric nanoformulation: uptake by cells and organs. *Int. J. Nanomed.* **2019**, *14*, 1−15.
(90) Fülöp, Z.; Gref, R.; Loftsson, T. A permeation method for detection of self-aggregation of doxorubicin in aqueous environment. *Int. J. Pharm.* **2013**, *454*, 559−561.
(91) Gocheva, G.; Ilieva, N.; Peneva, K.; Ivanova, A. Characterization of the interaction forces in a drug carrier complex of doxorubicin with a drug-binding peptide. *Chem. Biol. Drug Des.* **2018**, *91*, 874−884.
(92) Piasentin, N.; Milotti, E.; Chignola, R. The control of acidity in tumor cells: A biophysical model. *Sci. Rep.* **2020**, *10*, 13613.
(93) Yoo, J.; Won, Y.-Y. Phenomenology of the initial burst release of drugs from PLGA microparticles. *ACS Biomater. Eng.* **2020**, *6*, 6053−6062.
(94) Park, M.-K.; Jun, S.; Kim, I.; Jin, S.-M.; Kim, J.-G.; Shin, T. J.; Lee, E. Stepwise drug-release behavior of onion-like vesicles generated from emulsification-induced assembly of semicrystalline polymer amphiphiles. *Adv. Funct. Mater.* **2015**, *25*, 4570−4579.
(95) Pourjavadi, A.; Tehrani, Z. M. Poly (N-isopropylacrylamide)-coated β-cyclodextrin-capped magnetic mesoporous silica nanoparticles exhibiting thermal and pH dual response for triggered anticancer drug delivery. *Int. J. Polym. Mater. Polym. Biomater.* **2017**, *66*, 336−348.
(96) Wu, J.; Zhang, Z.; Gu, J.; Zhou, W.; Liang, X.; Zhou, G.; Han, C. C.; Xu, S.; Liu, Y. Mechanism of a long-term controlled drug release system based on simple blended electrospun fibers. *J. Controlled Release* **2020**, *320*, 337−346.
(97) Cam, M. E.; Yildiz, S.; Alenezi, H.; Cesur, S.; Ozcan, G. S.; Erdemir, G.; Edirisinghe, U.; Akakin, D.; Kuruca, D. S.; Kabasakal, L.; Gunduz, O.; Edirisinghe, M. Evaluation of burst release and sustained release of pioglitazone-loaded fibrous mats on diabetic wound healing: an in vitro and in vivo comparison study. *J. Royal Soc. Interface.* **2020**, *17*, 20190712.
(98) Paszek, M. J.; Zahir, N.; Johnson, K. R.; Lakins, J. N.; Rozenberg, G. I.; Gefen, A.; Reinhart-King, C. A.; Margulies, S. S.; Dembo, M.; Boettiger, D.; Hammer, D. A.; Weaver, V. M. Tensional homeostasis and the malignant phenotype. *Cancer Cell* **2005**, *8*, 241−54.
(99) Ulrich, T. A.; de Juan Pardo, E. M.; Kumar, S. The Mechanical Rigidity of the Extracellular Matrix Regulates the Structure, Motility and Proliferation of Glioma Cells. *Cancer Res.* **2009**, *69*, 4167−4174.
(100) Engelhard, H. H.; Duncan, H. A.; Dal Canto, M. Molecular characterization of glioblastoma cell differentiation. *Neurosurgery* **1997**, *41*, 886−897.
(101) Thul, P. J.; Lindskog, C. The human protein atlas: A spatial map of the human proteome. *Protein Sci.* **2018**, *27*, 233−24.
(102) Kolb, M.; Kurz, S.; Schafer, A.; Huse, K.; Dietz, A.; Wichmann, G.; Birkenmeier, G. Verification and characterization of an alternative low density lipoprotein receptor-related protein 1 splice variant. *Plos One. 12* **2017**, *6*, e0180354.
(103) Lewis, C. A.; Brault, C.; Peck, B.; Bensaad, K.; Griffiths, B.; Mitter, R.; Chakravarty, P.; East, P.; Dankworth, B.; Alibhai, D.; Harris, L.; Schulze, A. SREBP maintains lipid biosynthesis and viability of cancer cells under lipid-and oxygen deprived conditions and defined a gene signature associated with poor survival in glioblastoma multiforme. *Oncogene.* **2015**, *34*, 5128−5140.
(104) Porkoláb, G.; Mészáros, M.; Tóth, A.; Szecskó, A.; Harazin, A.; Szegletes, Z.; Ferenc, G.; Blastyák, A.; Mátés, L.; Rákhely, G.; Deli, M. A.; Veszelka, S. Combination of alanine and glutathione as targeting ligands of nanoparticles enhances cargo delivery into the cells of the neurovascular Unit. *Pharmaceuticals* **2020**, *12*, 635.
(105) Meszaros, M.; Porkolab, G.; Kiss, L.; Pilbat, A.-M.; Kota, Z.; Kupihar, Z.; Keri, A.; Galbacs, G.; Siklos, L.; Toth, A.; Fulop, L.; Csete, M.; Sipos, A.; Hulper, P.; Sipos, P.; Pali, T.; Rakhely, G.; Szabo-Revesz, P.; Deli, M. A.; Veszelka, S. Niosomes decorated with dual ligands targeting brain endothelial transporters increase cargo penetration across the blood-brain barrier. *Eur. J. Pharm. Sci.* **2018**, *123*, 228−240.
(106) Watanabe, D.; Nakagawa, S.; Morofuji, Y.; Toth, A. E.; Vastag, M.; Aruga, J.; Niwa, M.; Deli, M. Characterization of a primate blood-brain barrier co-culture model prepared for primary brain endothelial cells, pericytes and astrocytes. *Pharmaceutics.* **2021**, *13*, 1484.
(107) Song, Y.; Du, D.; Li, L.; Xu, J.; Dutta, P.; Lin, Y. In vitro study of receptor-mediated silica nanoparticles delivery across blood-brain barrier. *ACS Appl. Mater. Interfaces.* **2017**, *9*, 20410−20416.
(108) On, N. H.; Mitchell, R.; Savant, S.; Bachmeier, C.; Hatch, G.; Miller, D. Examination of blood-brain barrier (BBB) integrity in a mouse brain tumor model. *J. Neuro. Oncol.* **2013**, *111*, 133−143.
(109) Mizutani, H.; Tada-Oikawa, S.; Hiraku, Y.; Kojima, M.; Kawanishi, S. Mechanism of apoptosis induced by doxorubicin through the generation of hydrogen peroxide. *Life Sci.* **2005**, *76*, 1439−1453.
(110) Rieger, A. M.; Nelson, K. L.; Konowalchuk, J. D.; Barreda, D. R. Modified Annexin V/Propidium Iodide Apoptosis Assay for Accurate Assessment of Cell Health. *J. Vis. Exp.* **2011**, *50*, 2597.
(111) Picardo, M.; Passi, S.; Sirianni, M.C.; Fiorilli, M.; Russo, G.D.; Cortesi, E.; Barile, G.; Breathnach, A.S.; Nazzaro-Porro, M. Activity of azelaic acid on cultures of lymphoma and leukemia-derived cell lines, normal resting and stimulated lymphocytes and 3T3 fibroblasts. *Biochem. Pharmacol.* **1985**, *34*, 1653−1658.
(112) Brüningk, S. C.; Rivens, I.; Box, C.; Oelfke, U.; ter Haar, G. 3D tumour spheroids for the prediction of the effects of radiation and hyperthermia treatments. *Sci. Rep.* **2020**, *10*, 1653.
(113) Amaral, R. L. F.; Miranda, M.; Marcato, P. D.; Swiech, K. Comparative Analysis of 3D Bladder Tumor Spheroids Obtained by Forced Floating and Hanging Drop Methods for Drug Screening. *Front Physiol.* **2017**, *8*, 605.
(114) Wallace, D. I.; Guo, X. Properties of tumor spheroid growth exhibited by simple mathematical models. *Front. Oncol.* **2013**, *3*, 51.
(115) Mehta, G.; Hsiao, A. Y.; Ingram, M.; Luker, G. D.; Takayama, S. Opportunities and challenges for use of tumor spheroids as models to test drug delivery and efficacy. *J. Controlled Release* **2012**, *164*, 192−204.
(116) Niora, M.; Pedersbæk, D.; Münter, R.; de Val Weywadt, M. F.; Farhangibarooji, Y.; Andresen, T. L.; Simonsen, J. B.; Jauffred, L. Head-to-Head Comparison of the Penetration Efficiency of Lipid-Based Nanoparticles into Tumor Spheroids. *ACS Omega* **2020**, *5*, 21162−21171.
(117) Lin, R.-Z.; Chang, H.-Y. Recent Advances in three-dimensional multicellular spheroid culture for biomedical research. *Biotechnol. J.* **2008**, *3*, 1172−1184.
(118) Cui, X.; Hartanto, Y.; Zhang, H. Advances in multicellular spheroids formation. *J. R. Soc. Interface.* **2017**, *14*, 20160877.
(119) Ryu, N.-E.; Lee, S.-H.; Park, H. Spheroid culture system methods and applications for mesenchymal stem cells. *Cells.* **2019**, *8*, 1620.
(120) Adcock, A. F.; Trivedi, G.; Edmondson, R.; Spearman, C.; Yang, L. Three-Dimensional (3D) Cell Cultures in Cell-based Assays for in-vitro Evaluation of Anticancer Drugs. *J. Anal. Bioanal Technol.* **2015**, *6*, 3.
(121) Pattni, B. S.; Nagelli, S. G.; Aryasomayajula, B.; Deshpande, P. P.; Kulkarni, A.; Hartner, W. C.; Thakur, G.; Degterev, A.; Torchilin, V. P. Targeting of micelles and liposomes loaded with the Pro-Apoptotic Drug NCL-240 into NCI/ADR-RES cells in a 3D spheroid model. *Pharm. Res.* **2016**, *33*, 2540−2551.
(122) Kamiloglu, S.; Sari, G.; Ozdal, T.; Capanoglu, E. Guidelines for cell viability assays. *Food Frontiers.* **2020**, *1*, 332−349.
(123) Bratosin, D.; Mitrofan, L.; Palii, C.; Estaquier, J.; Montreuil, J. Novel fluorescence assay using calcein-AM for determination of human erythrocyte viability and aging. *Cytometry* **2005**, *66A*, 78−84.
(124) Dini, S.; Binder, B. J.; Fischer, S. C.; Mattheyer, C.; Schmitz, A.; Stelzer, E. H. K.; Bean, N.; Green, J. E. F. Identifying the necrotic zone boundary in tumour spheroids with pair- correlation functions. *R. Soc. Interface.* **2016**, *13*, 20160649.

https://doi.org/10.1021/acsomega.2c08049
ACS Omega 2023, 8, 12124−12143